

# Clinopyroxene/melt trace-element-partitioning in sodic alkaline magmas

Charles Beard<sup>a,\*</sup>, Vincent van Hinsberg<sup>a</sup>, John Stix<sup>a</sup>, Max Wilke<sup>b,c</sup>

<sup>a</sup>*Earth and Planetary Sciences, McGill University, 3450 University Street, Montreal, Québec, H3A 0E8, Canada*

<sup>b</sup>*Institut für Erd- und Umweltwissenschaften, Universität Potsdam, Golm, Germany*

<sup>c</sup>*Chemie und Physik der Geomaterialien, Deutsches GeoForschungsZentrum GFZ, Potsdam, Germany*

---

## Abstract

Clinopyroxene is a key fractionating phase in alkaline magmatic systems, but its impact on metal-enrichment processes, and the formation of REE + HFSE mineralisation in particular, are not well understood. To constrain the control of clinopyroxene on REE + HFSE behaviour in sodic (per)alkaline magmas, a series of internally heated pressure vessel experiments was performed to determine clinopyroxene-melt element-partitioning systematics. Synthetic tephriphonolite to phonolite compositions were run  $\text{H}_2\text{O}$ -saturated at 650–825°C with oxygen fugacity buffered to  $\log f\text{O}_2 \approx \Delta\text{QFM} + 1$  or  $\log f\text{O}_2 \approx \Delta\text{QFM} + 5$ . Clinopyroxene-glass pairs from basanitic to phonolitic fall deposits from Tenerife, Canary Islands, were also measured to complement our experimentally derived data set.

The REE partition coefficients are 0.3–53, typically 2–6, with minima for high-aegirine clinopyroxene. Diopside-rich clinopyroxene ( $\text{Ae}_{5--25}$ ) prefer the

---

\*corresponding author

Email address: [charles.beard@mail.mcgill.ca](mailto:charles.beard@mail.mcgill.ca) (Charles Beard)

MREE and have high REE partition coefficients ( $D_{Eu}$  up to 53,  $D_{Sm}$  up to 47). As clinopyroxene become more Na- and less Ca-rich (Ae<sub>25--50</sub>), REE incorporation becomes less favourable, and both the M1 and M2 sites expand (to 0.79 Å and 1.12 Å), increasing  $D_{LREE}/D_{MREE}$ . Above Ae<sub>50</sub>, both M sites shrink slightly and HREE ( $V^I r_i \leq 0.9 \text{ \AA} \approx \text{Y}$ ) partition strongly onto the M1 site, consistent with a reduced charge penalty for REE  $\leftrightarrow$  Fe<sup>3+</sup> substitution.

Our data, complemented with an extensive literature database, constrain a model that predicts trace-element-partition coefficients between clinopyroxene and silicate melt using only mineral major-element compositions, temperature and pressure as input. The model is calibrated for use over a wide compositional range and can be used to interrogate clinopyroxene from a variety of natural systems to determine the trace-element concentrations in their source melts, or to forward model the trace-element evolution of tholeiitic mafic to evolved peralkaline magmatic systems.

*Keywords:* rare earth elements, aegirine, experimental petrology, Canary Islands, phonolite, peralkaline

---

## **1. Introduction**

Sodic clinopyroxene appear to more readily incorporate REE than their calcic equivalents (Marks et al., 2004), but despite fractionation of these minerals, melts in evolved alkaline systems can attain high REE contents, even up to economic levels (Kogarko, 1990; Downes et al., 2005; Marks et al., 2011; Sjöqvist et al., 2013; Goodenough et al., 2016; Möller and Williams-Jones, 2016). Trace-element data may be used to model magmatic processes (Spera and Bohrson, 2001; Troll and Schmincke, 2002; Boudreau, 2004; Xu et al., 2010; Girnis et al., 2013; Mungall and Brenan, 2014), but their interpretation requires precise knowledge of mineral/liquid element-partition coefficients. The approach has been applied to studies of mafic systems and mantle melting processes (Niu, 2004; Workman and Hart, 2005; Foley et al., 2013; Coumans et al., 2016; Peters et al., 2017). However, poor constraints on element-partitioning behaviour in alkaline and peralkaline rocks thus far preclude widespread application in these systems.

Experimental investigations of element-partitioning behaviour in alkali-enriched systems are limited in terms of composition (Wood and Trigila, 2001; Huang et al., 2006), and none yet have explored peralkaline conditions where molar  $(\text{Na}+\text{K})/\text{Al}$  exceeds 1. Additional information has been obtained from natural samples by measuring the concentration ratios of phenocryst–glass pairs from volcanic and intrusive rocks (Larsen, 1979; Wörner et al., 1983; Shearer and Larsen, 1994; Severs et al., 2009; Fedele et al., 2009; Mollo et al., 2016). However, these results may be biased by the presence of melt inclusions, mineral inclusions and mineral zoning, and their interpretation is commonly complicated by unknown or poorly constrained P-T-H<sub>2</sub>O-*f*O<sub>2</sub> con-

<sup>26</sup> ditions of equilibration and assumptions of closed-system behaviour.

<sup>27</sup> In this contribution, we present partition coefficients for sodic clinopyrox-  
<sup>28</sup> ene and silicate melts of tephriphonolite to phonolite composition, as deter-  
<sup>29</sup> mined from internally heated pressure vessel experiments on synthetic and  
<sup>30</sup> natural compositions. These are complemented by well-constrained natural  
<sup>31</sup> volcanic phenocryst-glass pairs from Canary Islands pyroclastic fall deposits.  
<sup>32</sup> We characterise the mineral compositional controls on element-partitioning  
<sup>33</sup> behaviour and present a predictive model for clinopyroxene/melt element-  
<sup>34</sup> partitioning that can be used to generate clinopyroxene/melt partition coef-  
<sup>35</sup> ficients using only clinopyroxene major-element compositions (e.g., as mea-  
<sup>36</sup> sured by electron-microprobe). This approach permits forward modelling of  
<sup>37</sup> element budgets during differentiation processes in magmatic systems, in-  
<sup>38</sup> cluding evolved sodic alkaline systems, as well as providing a mineral-based  
<sup>39</sup> tool that can be used to reconstruct parental melt compositions from clinopy-  
<sup>40</sup> roxene compositions in natural rocks.

## <sup>41</sup> 2. Methodology

### <sup>42</sup> 2.1. Experimental starting glasses

<sup>43</sup> pyroxene were synthesised in sodic alkaline melts of varying composition  
<sup>44</sup> to obtain a range of mineral compositions consistent with those in natu-  
<sup>45</sup> ral systems. Starting glass compositions are given in Table 1 and Figure  
<sup>46</sup> S1. Glasses L1 and L5 were prepared from reagent-grade oxide and carbon-  
<sup>47</sup> ate powders, ground together in an agate mortar, decarbonated for 6 hr at  
<sup>48</sup> 450°C, then homogenised in air for 3 hr at 1400°C in a Pt crucible. Repeated  
<sup>49</sup> fusion and grinding in agate ensured chemical homogeneity of the starting

glasses, which was confirmed by electron-microprobe analyses of the final fused glass. Finely ground Mud Tank zircon was added to the homogeneous major-element glasses as a source of Zr, Hf, Nb and Ta; the glasses were then fused for a further three hours at 1400°C. The remaining trace-elements were added as a cocktail of single element nitrate solutions (ICP-MS standards), dried onto the powdered glasses, then denitrified at 450°C for 30 minutes. The synthetic basanite L1 and phonolite L5 were mixed in varying proportions to make the low alkali (L) series of starting glasses, while dried NaOH and KOH powders were added to make the middle (M) and high (H) alkali starting glasses. Analyses of glass compositions L5 and H5, quenched from superliquidus conditions, confirm that Henry's law was respected (Supplement S1).

A well-mixed rock powder from the Nechalacho Layered Suite in Canada (Möller and Williams-Jones, 2016, Unit NLS-9, sample L09-194-405.5, alternative sample name VM 11-6) was used as experimental starting material for a more extreme peralkaline composition. This composition was not fused prior to loading into experiment capsules, so as to preserve the original volatile element concentrations. An experiment using this material that was quenched from superliquidus conditions is homogeneous with respect to major-elements, as determined from EPMA measurements.

## 2.2. Experimental equipment and procedures

In total, 36 partitioning experiments were conducted in a Harwood-type internally heated pressure vessel (IHPV) in the HP-GeoMatS laboratory at the German GeoForschungsZentrum (Table S1). Temperature was measured with Type-S thermocouples calibrated against the melting point of NaCl

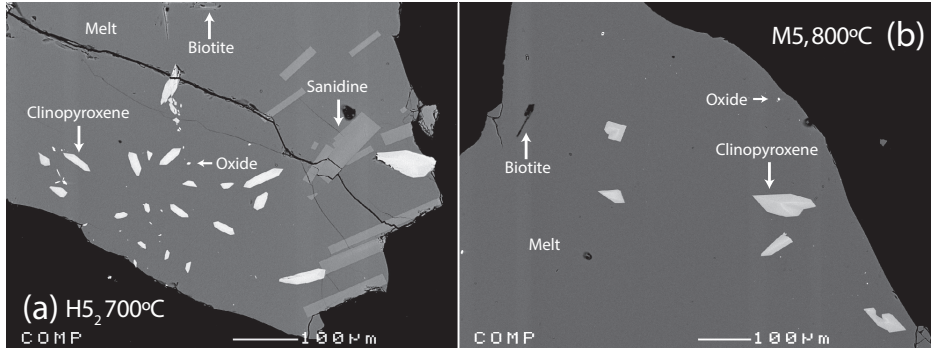


Figure 1: Backscattered electron images showing typical textures of run products from the internally heated pressure vessel experiments. Crystal fractions are typically small (<10% by area), with blade-shaped, euhedral clinopyroxene and glasses free of quench crystals.

(Borchert et al., 2010, accuracy of  $\pm 5$  °C at 200 MPa). Argon gas was used as the pressure medium, and pressure was measured with a strain gauge to an accuracy of  $\pm 7$  MPa. During the experiments, pressure was controlled automatically and held within  $\pm 5$  MPa of stated values.

Oxygen fugacity was buffered to the intrinsic redox conditions of the experimental setup, which corresponds to  $\log f\text{O}_2 \text{ ca. } \Delta\text{QFM} + 1$  in our  $\text{H}_2\text{O}$ -saturated charges (see Chou, 1986; Berndt et al., 2002; Jugo et al., 2010). One experiment using the Nechalacho Layered Suite composition was performed in a double capsule with a haematite solid buffer, designed to increase  $f\text{O}_2$  and promote crystallisation of  $\text{Fe}^{3+}$ -rich clinopyroxene (Eugster and Wones, 1962). This experiment ran at the Hm-Mt buffer, which corresponds to  $\log f\text{O}_2 \approx \Delta\text{QFM} + 5$ , as confirmed by presence of both buffer minerals in the outer capsule following quench. The experiments were designed to run between the liquidus and solidus for each composition, which corresponds to temperatures between 650 and 825°C, all at 200 MPa pressure (Table S1).

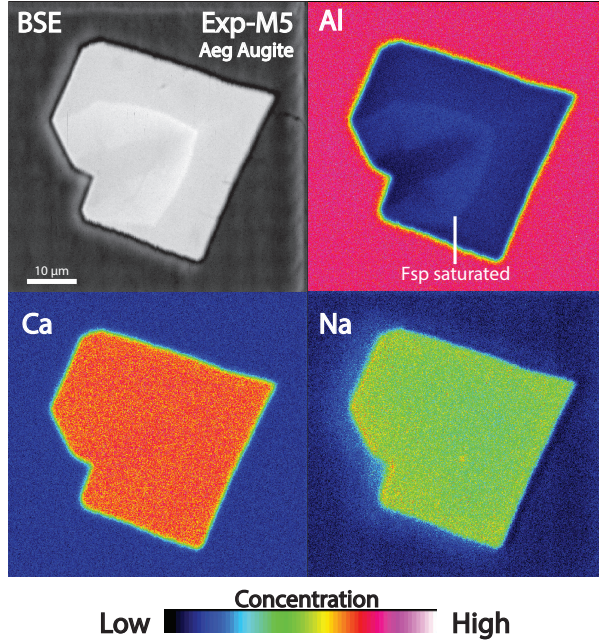


Figure 2: Element maps of clinopyroxene from internally heated pressure vessel experiment M5. Aegirine-augite clinopyroxene have a sharp internal boundary that reflects feldspar saturation and are subtly zoned. Further element maps are available as an electronic supplement (Fig. S2).

Powdered starting glass and distilled, deionised water were welded inside 90 3 or 3.5 mm outer diameter platinum capsules of 20–25 mm length (see Ta-  
 91 ble S1). To verify that capsules were sealed, they were heated to 110°C and  
 92 weighed before and after. The amount of water sealed inside the capsules  
 93 varied with temperature and composition and was kept in excess of sat-  
 94 uration (Carroll and Blank, 1997; Moore et al., 1998; Schmidt and Behrens,  
 95 2008). Water saturation was confirmed post-run by puncturing capsules and  
 96 checking for water expulsion and mass loss on drying at 110°C.  
 97

98        The capsules were loaded into the vessel, pressurised to 200 MPa, then  
99        heated to superliquidus temperatures for at least 16 h (Table S1) to per-  
100      mit homogenisation of trace-element concentrations, dissolution of water and  
101      equilibration of  $f\text{O}_2$  by exchange of  $\text{H}_2$  through the capsule wall (cf. Gaillard  
102      et al., 2002). Following homogenisation, temperature was lowered to run  
103      conditions. An initial set of experiments were cooled rapidly from homogeni-  
104      sation to run temperature at about 100°C/min. A second set of experiments  
105      were cooled to run temperature at 1°C/min to promote slow growth of crys-  
106      tals and to minimise the formation of compositional gradients in the melt.  
107      Vessel temperature was then cycled between run temperature and run tem-  
108      perature + 10°C to promote dissolution of small crystals at the expense of  
109      larger grains, and to promote crystal growth close to the run temperature.  
110      Element partitioning results are consistent among experiments of different  
111      cooling paths. In all experiments, run temperature was kept constant for at  
112      least 40 h to allow for chemical homogenisation of melt and growth of crystals  
113      via Ostwald ripening. Capsules were then quenched to room temperature.

114        To minimise the growth of groundmass crystals on cooling, a rapid quench  
115      apparatus was used where possible (Berndt et al., 2002, Table 2). We have  
116      not measured quench rates in this vessel, but the capsules probably cooled  
117      at rates in excess of 100°C/s. For the rest of the experiments, quenching  
118      was achieved by cutting power to the furnace, which resulted in cooling to  
119      below the glass-transition temperature (< 350°C; Giordano et al., 2005) in  
120      less than 150 s.

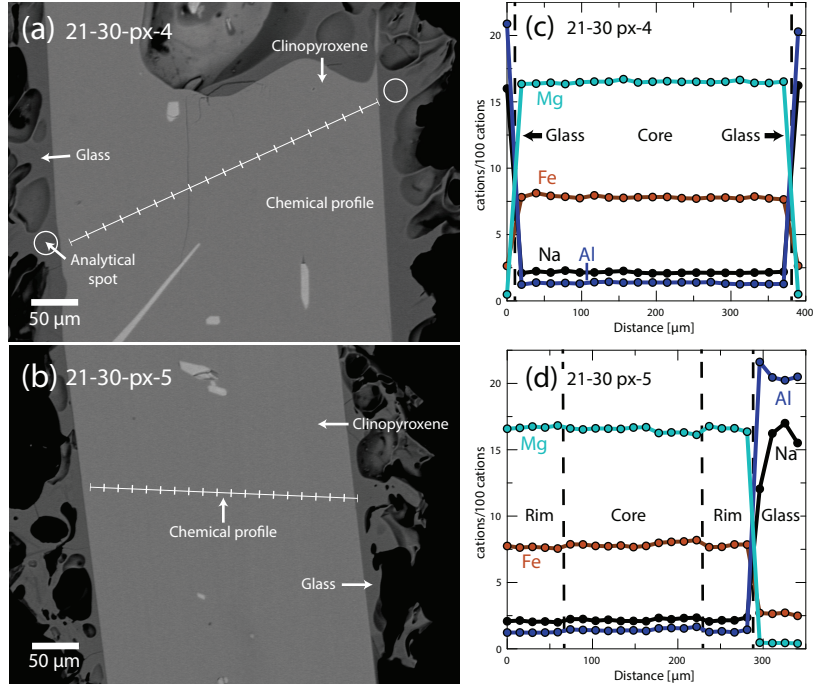


Figure 3: Examples of textural features from Canary Islands clinopyroxene phenocrysts from this study. (a, b) Backscattered electron images show that crystals are euhedral and are free from complex zoning patterns. (c, d) Chemical profiles across clinopyroxene phenocrysts and glass rims (quenched melt), as measured by wavelength dispersive spectroscopy, showing that zoning is effectively absent in these clinopyroxene. In (c) analyses of glass are aligned with the chemical profile shown in (a). Glass analyses shown in (d) are from rims of quenched melt from other clinopyroxene phenocrysts recovered from the same pumice sample. Both pictured phenocrysts are from the basal air fall deposit, associated with the ~2 ka eruption of Pico Viejo, Tenerife (Abhay et al., 1995).

121     *2.3. Natural samples*

122     Alkaline volcanism on Tenerife is associated with a weak thermal mantle  
 123     plume that impinges upon thick, old, slow-moving oceanic lithosphere (Car-  
 124     racedo et al., 2007). This geological scenario has favoured development of a

125 complex magma-plumbing system that produces a great diversity of volcanic  
126 products from alkali basalt to phonolite in composition. The Las Cañadas  
127 edifice, a large, central, composite stratovolcano (Bryan et al., 1998; Brown  
128 et al., 2003; Edgar et al., 2007) rests upon a base of at least three mafic al-  
129 kaline shield volcanoes (Thirlwall et al., 2000; Guillou et al., 2004; Gurenko  
130 et al., 2006). Xenoliths indicate that a nepheline syenite intrusive system  
131 underlies the island (Wiesmaier et al., 2012).

132 Six clinopyroxene/glass pairs from four different volcanic eruptions on  
133 Tenerife have been investigated. The  $\sim$  2 ka eruptive products of Montaña  
134 Blanca and Pico Viejo (Abhay et al., 1995) are phonolitic, plinian fall de-  
135 posits, whereas Montaña Samara is a monogenetic, mafic cinder cone (Albert  
136 et al., 2015). Phase-equilibrium experiments conducted on Montaña Blanca  
137 unit UMB-II suggest that magma was stored prior to eruption at  $850 \pm 15^\circ\text{C}$ ,  
138  $50 \pm 20$  MPa, with  $2.5 \pm 0.5$  wt% H<sub>2</sub>O at  $\log f\text{O}_2 \approx \text{NNO} - 0.5$  (Andújar and  
139 Scaillet, 2012). Field locations, mineral proportions and major-element com-  
140 positions of the clinopyroxene and glasses are presented in Table S1.

#### 141 2.4. Sample preparation

142 Experiment capsules were torn open with pliers, and charges were split  
143 using a low-speed wafering saw. Samples were mounted in epoxy resin and  
144 polished for *in situ* chemical analyses.

145 Natural pyroclastic rocks were rinsed in tap water and crushed with a  
146 hammer. Crystals and glass fragments, hand-picked from a sieved size-  
147 fraction between 1.18 mm and 125  $\mu\text{m}$ , were used to make grain mounts  
148 containing 5–20 crystals of clinopyroxene per sample. Natural samples also  
149 contain biotite, sanidine,  $\pm$  spinel, amphibole, olivine, titanite and sodalite.

<sub>150</sub> clinopyroxene mineral mounts were examined using backscattered electron  
<sub>151</sub> imaging to select euhedral crystals that were free from melt inclusions and  
<sub>152</sub> chemical zoning ( $n = 6$ , Fig. 3).

<sub>153</sub> **3. Analytical techniques**

<sub>154</sub> All experimental products were examined by reflected light optical mi-  
<sub>155</sub> croscopy and SEM, and all phases produced were identified by electron-  
<sub>156</sub> microprobe using an energy-dispersive detector. Images were obtained to  
<sub>157</sub> estimate modal proportions of phases, which were calculated using ImageJ  
<sub>158</sub> freeware (Rasband, 2016, see Table S1).

<sub>159</sub> *3.1. Electron-microprobe analysis*

<sub>160</sub> Major-element compositions of experimental products and natural min-  
<sub>161</sub> erals and glasses were measured with a JEOL 8900 instrument at McGill  
<sub>162</sub> University and a JEOL 8230 instrument at the University of Ottawa (Table  
<sub>163</sub> 3). An accelerating voltage of 15 kV was used with a 15 nA beam of  $5 \mu\text{m}$   
<sub>164</sub> diameter for minerals, and a 4 nA beam of  $50 \mu\text{m}$  diameter for glasses. Count  
<sub>165</sub> times for all elements were 60 s. Using the above routine, we observed no  
<sub>166</sub> sodium loss over the measurement time period. For the silicate minerals and  
<sub>167</sub> glasses, both synthetic and natural minerals or oxides were used for calibra-  
<sub>168</sub> tion (see Table S1). Analytical uncertainties were determined by multiple  
<sub>169</sub> analyses of reference materials and duplicate analyses of samples.

<sub>170</sub> Element distribution maps were generated with a JEOL 8900 instrument  
<sub>171</sub> at McGill University using an accelerating voltage of 15 kV, a focussed 40  
<sub>172</sub> nA beam, and a dwell time of 50 ms per pixel (Figs. 2, S2). Fe, Ti, Al, Si

<sup>173</sup> and Na were measured with wavelength-dispersive detectors, while Ca and  
<sup>174</sup> Mg were measured with an energy-dispersive spectrometer.

<sup>175</sup> Transects of Ce, Mg and Fe concentrations within the experiment clinopy-  
<sup>176</sup> roxene were measured with a JEOL 8900 instrument at McGill University  
<sup>177</sup> using a focussed beam of 50 nA with an accelerating voltage of 20 kV. Ce  
<sup>178</sup> was counted with a wavelength-dispersive spectrometer with an LIFH crystal  
<sup>179</sup> for 100 s (MAC-Ce standard). Mg and Fe were counted for 20 s, with TAP  
<sup>180</sup> and LIF crystals respectively (diopside and olivine standards, respectively).  
<sup>181</sup> Matrix corrections for Mg, Fe and Ce were not possible with these data, for  
<sup>182</sup> lack of other major-elements measured, however their relative values may  
<sup>183</sup> still be used to assess the extent to which the clinopyroxene are chemically  
<sup>184</sup> zoned.

<sup>185</sup> *3.2. Laser-ablation ICP-MS*

<sup>186</sup> Trace-element concentrations of clinopyroxene and glasses were deter-  
<sup>187</sup> mined by laser-ablation ICP mass spectrometry. Analyses were performed  
<sup>188</sup> at McGill University using a NewWave 213 nm Nd-YAG laser system coupled  
<sup>189</sup> to a Thermo Finnigan iCAP-Qc quadrupole ICP-MS instrument. Typical flu-  
<sup>190</sup> ence was 3–12 J/cm<sup>2</sup> (from 80 µm to 8 µm spot sizes), with a repetition rate  
<sup>191</sup> of 10 Hz. Ablated material was transferred to the ICP-MS in a He flow of 800  
<sup>192</sup> mL/min and mixed with Ar prior to injection into the plasma. Instrumental  
<sup>193</sup> drift was monitored by repeat analyses of the primary standard glass BCR-  
<sup>194</sup> 2G, with bias monitored by repeat analyses of secondary standards UTR-2  
<sup>195</sup> peralkaline rhyolite and USGS-RGM-1 rhyolite glasses (Table S1). Sample  
<sup>196</sup> surfaces were pre-ablated to remove residues from polishing materials and to  
<sup>197</sup> improve ablation efficiency.

198 Primary and secondary standards and an unzoned Canary Islands clinopy-  
199 roxene were analysed with beam sizes of 8–80  $\mu\text{m}$  to monitor crater-size-  
200 dependent element-fractionation effects; none were found for the elements  
201 reported here. For minerals and glasses in the experimental charges, beam  
202 sizes of 8–40  $\mu\text{m}$  and 16–80  $\mu\text{m}$  were used, respectively. Depending on grain  
203 size and availability, 5–14 mineral grains and 3–10 areas of glass were anal-  
204 ysed per charge. Natural clinopyroxene and rim glasses were analysed using  
205 a beam size of 12–80  $\mu\text{m}$  and 12–30  $\mu\text{m}$ , respectively. Wherever possible,  
206 ablation was performed along lines parallel to crystal rims (1–3  $\mu\text{m} / \text{s}$ ).

207 Drift corrections and data reduction were conducted in Iolite v2.5 (Pa-  
208 ton et al., 2011). The total of major-elements measured by LA-ICP-MS  
209 or, where available, the Al concentration from electron-microprobe analyses,  
210 was used as an internal standard (Table 3). For some experiments, ablation  
211 through the minerals was too rapid to generate a stable signal for data-  
212 reduction purposes. In these cases, a mixing model was applied to estimate  
213 the composition of these clinopyroxene, similar to that applied by Rubatto  
214 and Hermann (2007) (see supplementary methods S4).

#### 215 4. Results

216 A total of 11 experiments are reported. Phase proportions, major-element  
217 and trace-element abundances in quenched melts and clinopyroxene are pro-  
218 vided in Table S1; 25 additional experiments were rejected as their run tem-  
219 peratures were superliquidus or subsolidus, or their growth textures were  
220 indicative of disequilibrium (e.g. Fig. S2).

221 All reported experimental runs were near-liquidus (<22% crystals), and

222 are characterised by a homogeneous distribution of phases (Fig 1), except for  
223 experiments H5<sub>3</sub> and NLS-9<sub>2-HM</sub>, in which sanidine crystals are concentrated  
224 at the centre. Glasses are clean and homogeneous, and clinopyroxene crystals  
225 are generally small, euhedral blades with a narrow range of sizes for a given  
226 experiment (<10 µm to 100 µm in cross section, Figs. 1–2).

227 Glasses are homogeneous and show a limited range of major- and trace-  
228 element compositions for each experiment (Fig. S1). In addition to clinopy-  
229 roxene and glass, experiments on mafic to intermediate compositions pro-  
230 duced magnetite, titanite ± kaersutite amphibole, whereas some phonolitic  
231 experiments produced biotite, alkali feldspar ± magnetite (Table S1).

232 Low sums of major-element oxide concentrations in the electron micro-  
233 probe analyses are a result of high Fe<sup>3+</sup> contents in the pyroxenes, and high  
234 water contents in the quenched melts (Supplement S1).

235 *4.1. Compositions of the clinopyroxene and major-element exchange*

236 The Canary Islands clinopyroxene are diopside<sub>60–90</sub>, with most crystals  
237 containing about 0.05 c.f.u. <sup>IV</sup>Al (in the T site) and 0.02 c.f.u. <sup>VI</sup>Ti (in  
238 the M1 site, Tables 3, S1, Fig. 4). Experiments on the synthetic compo-  
239 sitions produced clinopyroxene of diopside to aegirine-augite composition, a  
240 subset of which overlap with the compositional space defined by the Canary  
241 Islands on a diopside–hedenbergite–aegirine ternary diagram (Fig. 4a). This  
242 low-aegirine group of synthetic clinopyroxene display a positive correlation  
243 between <sup>IV</sup>Al and <sup>VI</sup>Ti content (red, *low aegirine*, Ae<sub>5–25</sub>), and notably con-  
244 tain both of these elements at elevated concentration relative to the Canary  
245 Islands clinopyroxene (<sup>IV</sup>Al = 0.20–0.45 c.f.u., <sup>VI</sup>Ti = 0.07–0.17 c.f.u.). A  
246 further subset of synthetic clinopyroxene have higher aegirine contents (blue,

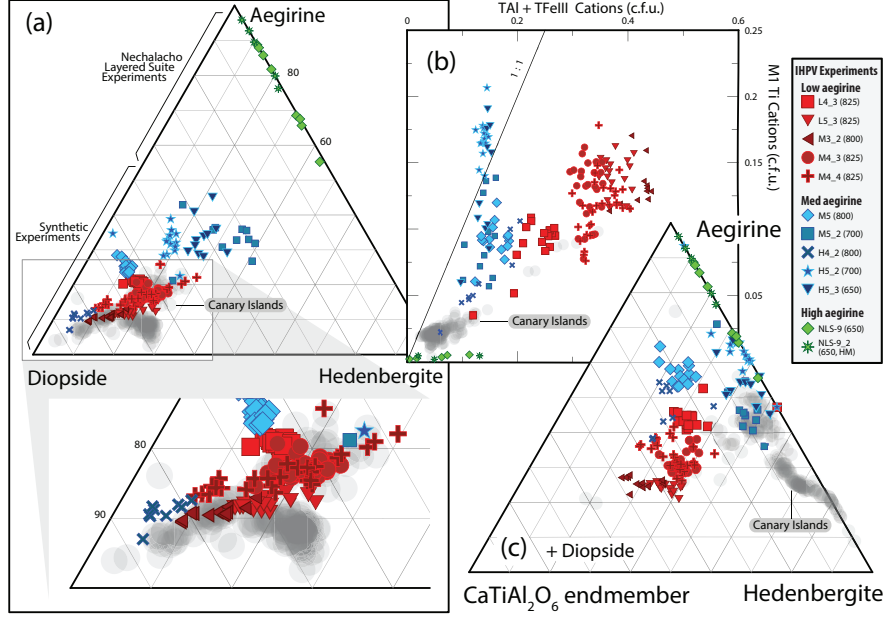


Figure 4: pyroxene grown in internally heated pressure vessel experiments (a) expressed in terms of diopside, hedenbergite and aegirine end-members, (b) their M1Ti and tetrahedral Al and  $\text{Fe}^{3+}$  contents, and (c) expressed in terms of aegirine, hedenbergite and the theoretical  $\text{CaTiAl}_2\text{O}_6$  end-member (Akasaka and Onuma, 1980). clinopyroxene compositions from Canary Islands volcanic rocks are shown for comparison (this study).  $\text{Fe}^{2+}/\text{Fe}^{3+}$  within the clinopyroxene was assigned following Droop (1987), then site occupancies and end-member proportions were allocated following Morimoto (1989). For full details on the end-member calculation procedure, see supplementary material. The range of clinopyroxene compositions within each experiment records ‘fractional crystallisation’ during the course of the experiment, whereby the cores of crystals become chemically isolated from the melt. The rims (highest Fe, Na) of each experiment are in equilibrium with the adjacent melt.

<sup>247</sup> *med aegirine,  $\text{Ae}_{25-50}$* ) and show a similar range of Ti contents to the low ae-  
<sup>248</sup> girine synthetic minerals (0.05–0.18 c.f.u.), but a limited range of lower  ${}^{\text{IV}}\text{Al}$   
<sup>249</sup> content (0.1–0.2 c.f.u.). Experiments performed on the Nechalacho layered

250 suite composition (NLS-9, NLS-9<sub>2-HM</sub>, green, *high aegirine*, Ae<sub>55--95</sub>) repro-  
251 duced the aegirine-augite to aegirine clinopyroxene from the natural system  
252 and contain almost no <sup>IV</sup>Al, <sup>VI</sup>Ti, Ca or Mg (Möller and Williams-Jones,  
253 2016).

254 The Canary Islands clinopyroxene that were selected for determination  
255 of mineral–melt partition coefficients are free from melt inclusions, suggest-  
256 ing relatively slow rates of crystal growth (Kennedy et al., 1993, Fig. 3).  
257 Chemical zonation, if present, is more subtle than the analytical precision  
258 of our electron microprobe, indicating that pressure, temperature and melt  
259 composition remained stable during crystal growth. In the case of these Ca-  
260 nary Islands clinopyroxene, the entire mineral is in chemical equilibrium with  
261 the adhered quenched melt. We are confident of this at a level greater than  
262 the analytical precision of electron microprobe analyses (typically ~2%). By  
263 contrast our experiment clinopyroxene display systematic compositional vari-  
264 ation between their cores and rims; this variation recording changes to melt  
265 composition during growth of these crystals (e.g. Fig. 2).

266 By definition, crystallisation changes the composition of the adjacent melt  
267 by preferentially removing compatible major-elements relative to those of  
268 lower compatibility, therefore all crystallisation induces some changes to melt  
269 composition.

270 This crystal-chemical zonation is systematic both within individual exper-  
271 iments and within groups of experiments and results from growth of crystals  
272 from a limited volume of melt within the experimental charges.

273 revealing three major-element exchange mechanisms. These exchange  
274 mechanisms correspond to low (Ae<sub>5--25</sub>), medium (Ae<sub>25--50</sub>) and high (Ae<sub>55--95</sub>)

275 aegirine domains defined above (Figs. 4b, 5 and S3). With increasing alkali  
276 content, the Si content of clinopyroxene increases at the expense of tetrahe-  
277 drally co-ordinated Al and Fe<sup>3+</sup>. As aegirine content increases, substitutions  
278 at the tetrahedral site become relatively less important than exchanges at the  
279 M1 and M2 sites. At the M1 site, the substitution of Ti for ions of 2+ and  
280 3+ valence correlates well with the exchange of tetrahedrally coordinated 3+  
281 cations for Si<sup>4+</sup>. The exchange behaviour of 2+ and 3+ cations at the M1  
282 site depends on the aegirine content of the clinopyroxene. In low-aegirine  
283 clinopyroxene, the concentration of 3+ ions at the M1 site is negatively cor-  
284 related with  $X_{Na}^{M2}$ , whereas in medium- and high-aegirine clinopyroxene, the  
285 M1 site takes progressively more 3+ ions as  $X_{Na}^{M2}$  increases. Substitutions of  
286 Ca<sup>M2</sup> for Na<sup>M2</sup> are relatively unimportant in low-aegirine clinopyroxene, but  
287 play a large role in medium- and high-aegirine exchange vectors.

288 Suites of Canary Islands clinopyroxene follow similar major-element ex-  
289 change systematics to our low aegirine experiment clinopyroxenes (CHECK).

290 Clinopyroxene has the general formula M2M1T<sub>2</sub>O<sub>6</sub>, with the M1 and M2  
291 sites incorporating most of the trace-elements of geological interest (Mor-  
292 imoto, 1989). Iron in the clinopyroxene was assigned to 2+ or 3+ valence  
293 following Droop (1987), then major-element cations were assigned to sites  
294 following Morimoto (1989, see supplement S5).

295  
296 The clinopyroxene crystals show a small range of major-element compo-  
297 sition in each experiment (Fig. 4).

298 Where large crystals were present and the mixing model was not required  
299 for reduction of laser-ablation data, trace-element compositions are similar

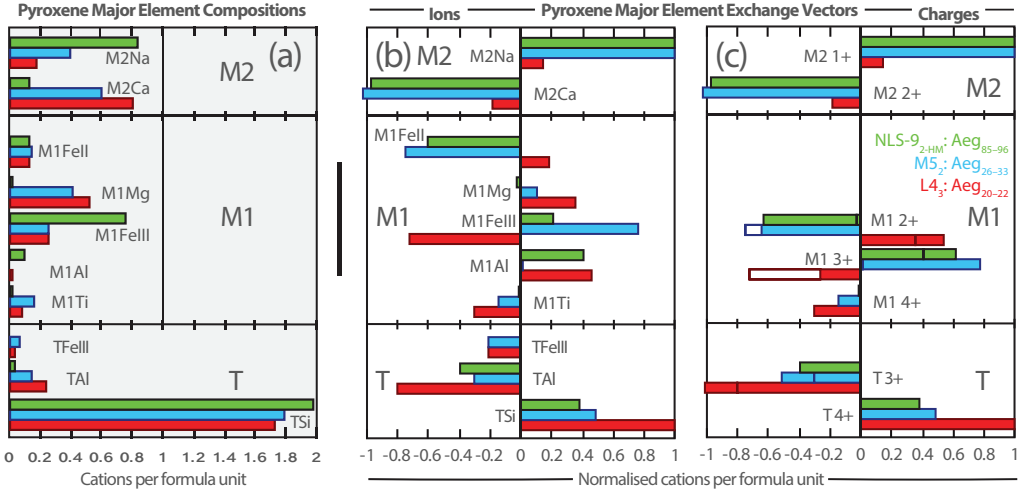


Figure 5: Bar charts showing clinopyroxene composition and major-element exchange mechanisms for three experiments representative of high (green), medium (blue) and low-aegirine (red) clinopyroxene. (a) clinopyroxene major-element compositions expressed as cations per six-oxygen formula unit (b) exchange mechanisms grouped by ions, (c) grouped by charges. Methods used to calculate these exchange mechanisms are available in the caption of Supplementary Figure S3.

300 among clinopyroxene crystals within individual experiments, indicating that  
 301 the trace-element concentration of the melt remained spatially homogeneous  
 302 throughout the experimental charges during the course of the experiments.

## 303 5. Discussion

### 304 5.1. Attainment of equilibrium

305 Experiments used to determine trace-element-partition coefficients must  
 306 have attained, or at least closely approached, chemical equilibrium. Reversal  
 307 experiments, where a clinopyroxene re-equilibrates with a melt, are unfor-  
 308 tunately not possible owing to sluggish diffusion of most elements through

309 the clinopyroxene structure (Van Orman et al., 2001). As the formation  
310 of clinopyroxene necessarily changes the composition of melt, all crystalli-  
311 sation experiments and natural clinopyroxene, strictly speaking only record  
312 true equilibrium conditions at their outermost rim. However, where zoning  
313 is limited, partition coefficients from non-rim compositions will still closely  
314 approach equilibrium.

315 Several lines of evidence indicate that our experiments preserve condi-  
316 tions close to chemical equilibrium. The experimental charges underwent  
317 small degrees of crystallisation ( $\leq 35\%$ ), resulting in small changes to liquid  
318 compositions during the run (Fig. S1). Consequently, in our experiments,  
319 clinopyroxene display only subtle chemical zonation and cover a small range  
320 of major-element compositions within each charge (Figs. 2, 4). Such a small  
321 range would not be expected if significant zoning were present, because the  
322 sectioning level of clinopyroxene varies on the polished surface and with it  
323 the relative contributions of core and rim in the analyzed volume. Because  
324 our results are consistent regardless of the cooling path that was used for  
325 the experiments (see Table S1), and further that quenched melts are free of  
326 chemical zonation (Fig. 2), we suggest that the melt composition remained  
327 homogeneous during crystallisation, and that kinetic effects associated with  
328 diffusion of elements toward or away from the crystal-melt interface (e.g.  
329 Lofgren et al., 2006) were smaller than the analytical precision of our setup.

330 Most experiments display a uniform distribution of crystals, suggesting  
331 that melts were homogeneous at the beginning of crystallisation, that ex-  
332 perimental charges ran under isothermal conditions, and that gravitational  
333 separation of crystals was minimal. As charges were fused at superliquidus

334 conditions for a minimum of 16 hrs, the H<sub>2</sub>O content of the melts should have  
335 been homogeneous and  $fH_2$  (thus  $fO_2$ ) equilibrated with the gas pressure  
336 medium on initiation of crystallisation (Gaillard et al., 2002).

337 Near-duplicate experiments M4<sub>3</sub> and M4<sub>4</sub> have similar phase relations  
338 , crystal compositions and glass compositions, despite running for different  
339 times (45 hr vs. 49 hr). Additionally, two experiments that varied only  
340 in fluorine content (M3<sub>0.3</sub>F, with 0.3 wt.% fluorine, and M3<sub>2</sub>, fluorine-free)  
341 also generated similar mineral compositions and have near-identical element-  
342 partitioning behaviour (Beard, 2018).

343 Most experiments produced euhedral crystals. Only those on NLS compo-  
344 sitions show hopper and swallowtail textures, indicative of diffusion-limited  
345 crystal growth (Walker et al., 1976; Lofgren, 1989; Shea and Hammer, 2013).  
346 Such textures record growth that was limited with respect to major-elements,  
347 and do not necessarily record equilibrium element-partition coefficients for  
348 trace-elements. Diffusion-limited growth theoretically converges apparent  
349 clinopyroxene partition coefficients toward unity (e.g. Blundy et al., 1998),  
350 suggesting that in these experiments, the partition coefficients in excess of  
351 one should be treated as minimum values, and those below as maxima. How-  
352 ever the trends in partitioning behaviour are in excellent agreement with our  
353 experiments that grew euhedral crystals, suggesting minimal disequilibria  
354 effects (see discussion of growth rates below and Mollo et al. 2013).

355 Canary Islands clinopyroxene were inspected under reflected light and by  
356 SEM. Only euhedral, blade-shaped crystals free of melt inclusions and chem-  
357 ical zonation were selected for analysis, and the corresponding quenched melt  
358 was in direct contact (Fig. 3). While equilibrium conditions are more chal-

359 lenging to confirm for a natural volcanic system, the euhedral forms, chemi-  
360 cal homogeneity of crystals, and congruency between samples from separate  
361 eruptions suggest that the crystals grew in a stable environment, and were  
362 not subject to chemical or physical perturbations during growth (Fig. 6).

363 *5.2. Chemical zonation in the experiment clinopyroxene*

364 Because trace-elements diffuse slowly through the clinopyroxene struc-  
365 ture relative to the melt (Van Orman et al., 2001; Zhang et al., 2010), no  
366 re-equilibration of trace-elements takes place on an experimental timescale.  
367 Only the very rim of an experimentally grown mineral can record equilib-  
368 rium conditions and the bulk crystal cannot. Experiments designed for the  
369 derivation of equilibrium partition coefficients ideally minimise bias by lim-  
370 iting the fraction of crystallisation, producing minerals that are as homoge-  
371 neous as possible. Currently available *in situ* analytical techniques, such as  
372 LA-ICP-MS and SIMS, are limited in terms of minimum beam-size to  $\sim$ 10  
373  $\mu\text{m}$ ; chemical zonation, however subtle, will be continuous from the core to  
374 the rim of the mineral. Consequently, no experimentally derived partition  
375 coefficients record equilibrium partition coefficients *sensu stricto*, but when  
376 properly conducted, will get close.

377 The trace-element data collected from our experiments, and from pub-  
378 lished studies, are average compositions for clinopyroxene that are zoned to  
379 varying degrees, the rims of which record equilibrium with the surrounding  
380 melt. In situ chemical analyses preferentially sample the mantle and rim of  
381 zoned crystals, because few analyses section a crystal perfectly through the  
382 core, resulting in a bias toward equilibrium mineral compositions.

383 We modelled a worst-case scenario to determine how strongly chemical

384 zoning in clinopyroxene can affect the resultant  $D$  values for trace-elements.  
385 If 20% of the melt crystallises as clinopyroxene only, and where the chemical  
386 analyses are truly averages of clinopyroxene composition, an incompatible  
387 element with a true equilibrium partition coefficient of 0.1 would return a  
388 measured partition coefficient of 0.09. For compatible elements with true  $D$   
389 values of  $\sim 10$ , measured partition coefficients can be a factor of 2–3 higher.

390 Variability in the concentration of Ti in clinopyroxene from experiment  
391 M3<sub>2</sub>, one of our most completely crystallised charges, suggests that this model  
392 strongly exaggerates the effect of chemical zoning on partition coefficients,  
393 relative to our experiments. If maximum and minimum concentrations of  
394 Ti in the clinopyroxene are used to calculate partition coefficients, the range  
395 of derived  $D_{Ti}$  values is 12–16. In our experiments, the trace-element com-  
396 position of the melt does not vary as much as in this worst-case scenario  
397 model, partially because additional mineral phases have crystallised along-  
398 side clinopyroxene. For example, in experiment M3<sub>2</sub>, the REE are compatible  
399 in clinopyroxene, but are incompatible in biotite and oxides (e.g. Mahood and  
400 Stimac, 1990; Schmidt et al., 1999). The REE have therefore been residually  
401 enriched by crystallisation of biotite and oxide minerals, while simultane-  
402 ously being depleted by crystallisation of clinopyroxene. These two compet-  
403 ing processes serve to minimise the effect of fractional crystallisation on the  
404 concentration of trace-elements in the melt and consequently their derived  
405 partition coefficients. This modelling considered, the experimental partition  
406 coefficients that we report for incompatible elements should be reliable within  
407 analytical uncertainty, whereas the  $D$  values for compatible elements should  
408 be considered as maxima, but are probably overestimated by no more than

409 30%.

410 In addition to the Ti analyses discussed above, we have measured Ce con-  
411 centrations via EPMA point transects across some of our experiment clinopy-  
412 roxene (Supplement S3). The transects reveal clinopyroxene Ce concentra-  
413 tions that follow both sector zoning and concentric growth zoning patterns,  
414 as recorded by the  $X\text{Mg}$  of the clinopyroxene. Ratios of average Ce counts /  
415 rim Ce counts that represent the difference between bulk crystal and rim mea-  
416 surements have a mean of  $\sim 1.25$ , ranging between 1.01 and 1.41, consistent  
417 with compatible behaviour of Ce and fractionation of the cores of clinopyrox-  
418 ene crystals away from the chemically active part of the crystallising system.  
419 The high values are found for the largest clinopyroxene crystals and in these,  
420 because of their size, we were able to avoid the cores in the analyses. Ce  
421 partition coefficients as reported in our data set are therefore overestimated  
422 by a maximum of  $\sim 25\%$ . The small magnitude of this growth zonation ef-  
423 fect, relative to the worst case model scenario discussed above suggests that,  
424 in the case of incompatible elements, the partition coefficients derived from  
425 our experiments will be within analytical uncertainty of the true equilibrium  
426 values, whereas for compatible elements, they would be well within an or-  
427 der of magnitude of true values. Furthermore, because our laser-ablation  
428 data are reduced via a robust regression scheme, elevated concentrations of  
429 compatible elements in the cores of concentrically zoned clinopyroxene crys-  
430 tals are not strongly represented in the derived clinopyroxene trace-element  
431 concentration of the mix (Fig. S4b). LA-ICP-MS partition coefficients that  
432 we present are therefore less strongly biased toward high values than the  
433 25% value suggested by the EPMA data for Ce discussed above. Finally, as-

434 suming that equilibrium partitioning takes place throughout growth, zoning  
435 predominantly affects absolute  $D_i$  values, whereas the relationship between  
436  $D_i$  values and P, T and mineral composition are preserved. Zoning therefore  
437 does not impact our conclusions on the crystal-chemical and P-T controls on  
438 partitioning, nor the models that we derive for this. It would merely move  
439 absolute values by up to 25% for compatible elements.

440 *5.3. Variations in cooling rate and the formation of diffusive boundary layers*

441 During crystallisation a diffusive boundary layer develops within the melt  
442 directly adjacent to the growing minerals. Theoretically, this layer is depleted  
443 with respect to compatible elements and enriched with respect to those that  
444 are incompatible (Lu et al., 1995). The composition of a boundary layer  
445 depends on both the relative enrichment or depletion of elements during the  
446 crystallisation process, and the speed at which these elements diffuse through  
447 the melt. Rapidly diffusing elements with partition coefficients close to unity  
448 will have concentrations closest to that of the bulk melt.

449 Experiments designed to investigate trace-element-partitioning behaviour  
450 might employ slow cooling rates to limit the development of diffusive bound-  
451 ary layers, thus forming crystals from melt that is closer in composition to  
452 that of the bulk experiment. Such experiments then run into another prob-  
453 lem, in that significant crystallisation may occur at temperatures above that  
454 of the final run temperature. Rapidly cooled experiments circumnavigate  
455 this issue, but may form diffusive boundary layers during crystal growth that  
456 become ‘flattened out’ during the homogenisation stage of the experiment.

457 Numerous diffusion data have been gathered for silicate melts over the  
458 past few decades, and a comprehensive review is given by Zhang et al.

459 (2010). Diffusion of trace-elements through water-saturated peralkaline melts  
460 is rapid, owing to their depolymerised structure. For example La diffusion  
461 coefficients are 6 orders of magnitude higher than for granitic compositions of  
462 a similar temperature (compare Rapp and Watson, 1986; Behrens and Hahn,  
463 2009). This rapid diffusion serves to minimise the formation of diffusive  
464 boundary layers adjacent to growing crystals in our experiments. Coupled  
465 diffusion mechanisms complicate the application measured of single-element  
466 diffusion coefficients to a crystallising system (Grove et al., 1984; Liang et al.,  
467 1994; Costa et al., 2003). Here, the diffusive flux of trace-elements may be  
468 coupled to gradients in major-element concentration within the melt.

469 To investigate the impact of diffusive effects on trace-element-partitioning  
470 between clinopyroxene and melt, Mollo et al. (2013) performed crystallisation  
471 experiments on trachybasaltic melts at a range of cooling rates ( $2.5\text{--}50^{\circ}\text{C} / \text{hr}$ ). Rapid cooling rates result in depletions of Si, Ca and Mg in the clinopy-  
472 roxene that are compensated for by enrichments in Al, Na and Ti. Regardless  
473 of cooling rate, Ounma parabolae could be fitted through isovalent sets of  
474 partition coefficients, indicating that crystal lattice effects dominated over  
475 those associated with the formation of diffusive boundary layers and that  
476 local equilibrium was achieved at the time of crystallisation. In their rapidly  
477 cooled experiments, Mollo et al. (2013) found apparent clinopyroxene/melt  
478 trace-element-partition coefficients that varied within the same order of mag-  
479 nitude as true equilibrium partition coefficients, both following clinopyroxene  
480 composition (*ibid.* Fig. 9). Deviations of the partition coefficient of several  
481 orders of magnitude can be obtained only when rapidly growing crystals en-  
482 trap small portions of the diffusive boundary layer that are found as minute  
483

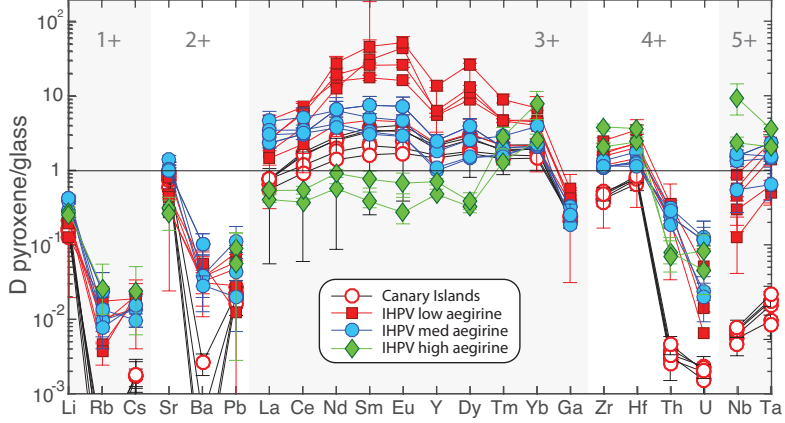


Figure 6: Trace-element-partition coefficients between clinopyroxene and melts, as determined from internally heated pressure vessel experiments ( $n = 11$ ) and from clinopyroxene-rim glass pairs from pyroclastic fall deposits from Tenerife, Canary Islands ( $n = 6$ ). Uncertainties on the partition coefficients are  $1\sigma$ .

melt inclusions randomly distributed in the mineral phase (Kennedy et al., 1993). In this case, partitioning behaviour is obviously influenced by contamination phenomena and no Onuma parabolas can be derived. As Onuma parabolae could successfully be fitted through partitioning data for all of our presented experiments (see following sections), and no melt inclusions were observed in optical and electron imaging, we infer that our data were not affected by the presence of such melt inclusions, and that they may be compared directly with partitioning data derived from experiments that employed slower cooling rates.

#### 5.4. Trace-element-partitioning

Element-partition coefficients and their uncertainties are reported in Tables 4 and S1. Uncertainty calculations are described in the caption for Figure

496 S4. Three markedly different behaviours of rare earth element-partitioning  
497 are observed in the experiments and Canary Islands rocks (Fig. 6). These de-  
498 pend on the aegirine concentration in the clinopyroxene and match the major-  
499 element exchange vector domains discussed above. Low-aegirine clinopyrox-  
500 ene ( $Ae_{5--25}$ ), including those from the Canary Islands , prefer the MREE;  
501 medium-aegirine clinopyroxene ( $Ae_{25--50}$ ) show a similar behaviour, save  
502 for higher LREE partition coefficients, whereas high-aegirine clinopyroxene  
503 ( $Ae_{55--95}$ ) strongly prefer HREE and show incompatible behaviour for the  
504 light and middle REE. The REE partition coefficients are 0.3–53, typically  
505 2–6, with minima for LREE and MREE in high-aegirine clinopyroxene (Fig.  
506 6). Our experimental partition coefficients are about an order of magnitude  
507 higher than in most other studies of clinopyroxene-melt element-partitioning  
508 that were performed on different bulk compositions (Fig. 7d,e,f), with the  
509 exception of high Si systems, such as the Bandelier Tuff (cf. Olin and Wolff,  
510 2010). Canary Islands clinopyroxene have absolute REE partition coeffi-  
511 cients about one order of magnitude lower than our low-aegirine experimental  
512 clinopyroxene.

513 The high field-strength elements (HFSE) Zr, Hf, Nb and Ta are compati-  
514 ble to slightly incompatible in the experimental clinopyroxene, and typically  
515 1–2 orders of magnitude less compatible in the Canary Islands clinopyrox-  
516 ene (Fig. 7a,b,c). The HFSE are most compatible in sodic clinopyroxene.  
517 Partition coefficients for the large-ion lithophile elements K, Sr, Pb are pos-  
518 itively correlated with  $X_{Na}^{M2}$  in the low- and medium-aegirine clinopyroxene,  
519 but are lower in high-aegirine clinopyroxene (Fig. S5). The Rb, Cs and Ba  
520 partition coefficients have a high uncertainty and are maximum estimates

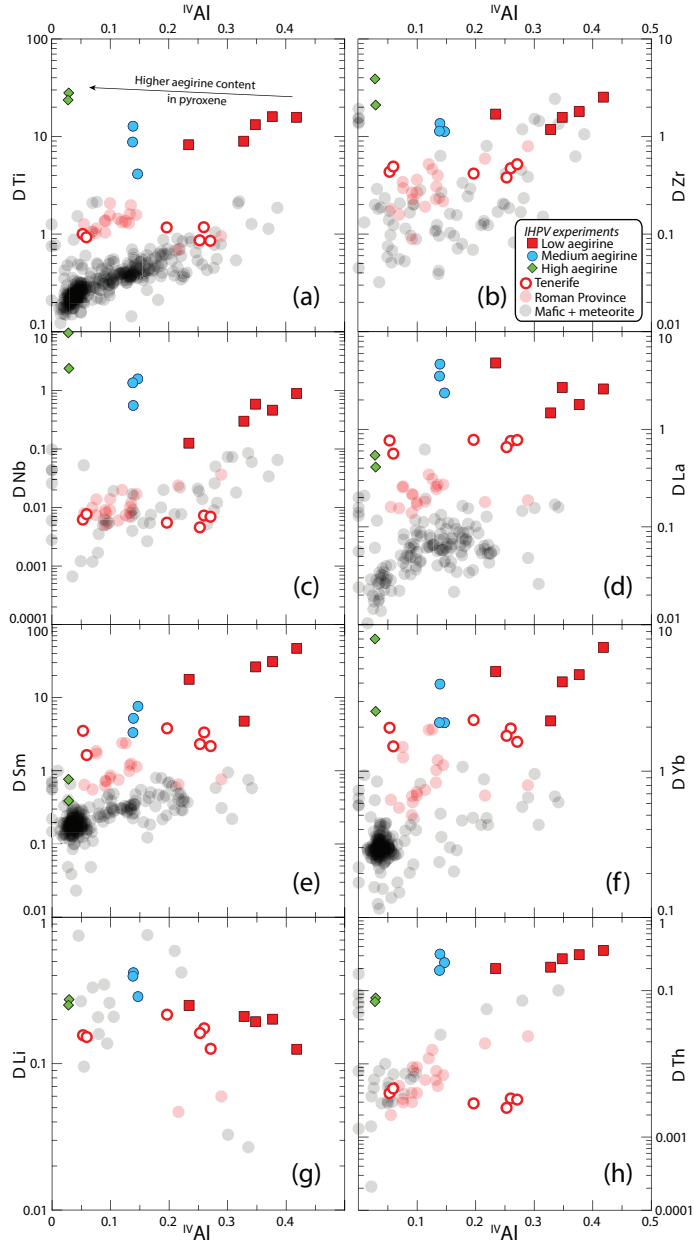


Figure 7: Element partition coefficients for HFSE (Ti, Zr, Nb), REE (La, Sm, Yb) and TE (Li, Th) vs.  $^{IV}\text{Al}$ . Literature values ( $n = 411$ ), including those from the Roman Province, Italy, are from the compilation of Bédard (2014), with additional, more recent, data from Mollo et al. (2016). A similar diagram with  $X_{\text{Na}}^{M2}$  in place of  $^{IV}\text{Al}$  is in Supplement S5.

owing to low concentrations of these elements in the clinopyroxene, close to the detection limit for analyses by LA-ICP-MS. These data are therefore not discussed further. Lithium is incompatible ( $D_{Li} = 0.1\text{--}0.4$ ) in both Canary Islands and experimental clinopyroxene and, like Sr and Pb, becomes more compatible with increasing aegirine content in the clinopyroxene, plateauing at  $X_{Na}^{M2} = 0.4$  and decreasing thereafter (Figs. 7g, S5g). The actinides U and Th show contrasting partitioning behaviour; the former showing no correlation with aegirine content in the clinopyroxene, the latter becoming more incompatible with increasing aegirine content (Fig. 7h). The U and Th partition coefficients for our Canary Islands samples are similar to those for the Roman Province (Wood and Trigila, 2001; Fedele et al., 2009; Mollo et al., 2013, 2016), and are 1–2 orders of magnitude more incompatible relative to the experimental clinopyroxene.

### 5.5. Fits to the lattice-strain model

The equilibrium partitioning of trace-elements between minerals and melts is largely controlled by the structure of the crystal lattice, its elasticity (Onuma et al., 1968; Kumazawa, 1969; Weidner and Vaughan, 1982) and its ability to accommodate an excess or shortage in charge (Blundy et al., 1998; Wood and Blundy, 2001; Hanchar et al., 2001; Corgne and Wood, 2005). The lattice-strain model provides a framework in which the influence of these variables on partitioning behaviour can be quantified, and thus predicted under conditions bracketed by a calibrating data set (Onuma et al., 1968; Blundy and Wood, 1994; Wood and Blundy, 2014). Lattice structure has a dependence on pressure, temperature and composition, and element-partitioning is a thermodynamically controlled process (e.g. Wood and Blundy, 1997).

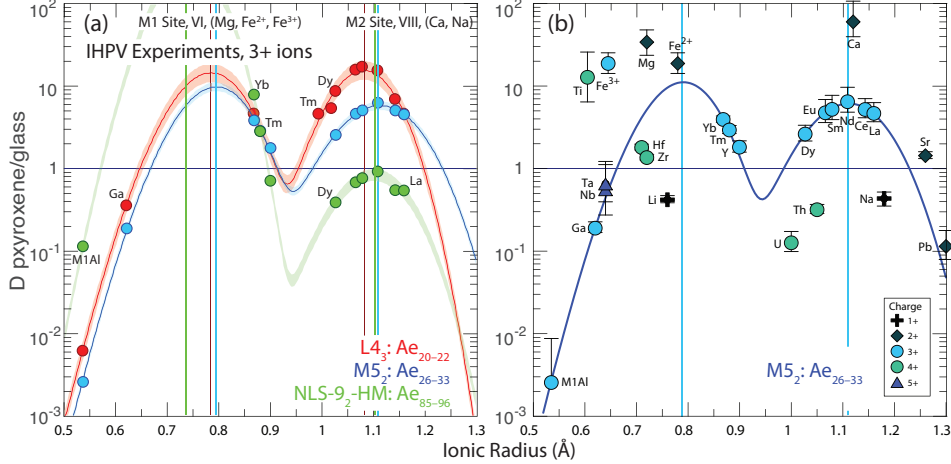


Figure 8: Non-linear weighted least-squares fits to element-partitioning data from the internally heated pressure vessel experiments following the lattice-strain model of Blundy and Wood (1994). (a) Representative fits to 3+ ion partitioning behaviour with examples for low, medium and high-aegirine clinopyroxene experiments. (b) Measured partition coefficients for ions of 1+, 2+, 4+ and 5+ charges that are consistent with the lattice-strain model. Ionic radii are assigned to 6 or 8 fold co-ordination (Shannon, 1976), and were chosen to minimise residuals in the fit (cf. Olin and Wolff, 2010). Y was not included in the fitting routine for 3+ ions because of mass fractionation effects (ibid.). Vertical coloured lines indicate ideal ionic radii ( $r_0$ ) of M1 and M2 sites and shaded areas indicate 95% confidence intervals on the fits determined via bootstrapping. Uncertainties on the partition coefficients in (b) are  $1\sigma$ . Fitted lattice-strain parameters are given in Table 4.

546 Most trivalent ions, including the REE and Y enter the larger M2 site  
 547 of clinopyroxene, which is typically 6- or 8-coordinated (Deer et al., 1992).  
 548 Smaller trivalent ions, including Al, Cr, Ga, Sc, and in the case of Fe-rich  
 549 clinopyroxene the HREE may enter the smaller, octahedral M1 site (Olin  
 550 and Wolff, 2010; Bédard, 2014). The high field-strength elements Ti, Zr, Hf,

551 Nb and Ta are typically hosted by the M1 site (Hill et al., 2000, 2011; Dygert  
 552 et al., 2014).

553 To investigate systematics in  $D_i$  values and the mechanisms by which  
 554 trace-elements are incorporated into clinopyroxene, element-partitioning be-  
 555 haviour was explored in light of the lattice-strain theory, quantitatively de-  
 556 scribed by the lattice-strain equation:

$$D_i^{mineral/melt} = D_0 \exp \left[ \frac{-4\pi E_s N_a}{RT} \left( \frac{r_0}{2} (r_0 - r_i)^2 - \frac{1}{3} (r_0 - r_i)^3 \right) \right] \quad (1)$$

557 where  $r_0$  is the ideal radius for the lattice site,  $E_s$  is the Young's modulus  
 558 (i.e., the lattice site stiffness),  $D_0$  is the strain-free partition coefficient,  $N_a$  is  
 559 Avagadro's number,  $R$  is the gas constant,  $T$  is temperature in Kelvin, and  
 560  $r_i$  is the ionic radius of the element in question, all radii in Å. We focused on  
 561 3+ ions that cover a wide range of radii and fitted lattice-strain parameters  
 562 for both the M1 and M2 sites of clinopyroxene (Fig. 8):

$$D_i^{cpx/melt} = D_0^{M2} \exp \left[ \frac{-4\pi E_s^{M2} N_a}{RT} \left( \frac{r_0^{M2}}{2} (r_0^{M2} - r_i)^2 - \frac{1}{3} (r_0^{M2} - r_i)^3 \right) \right] + D_0^{M1} \exp \left[ \frac{-4\pi E_s^{M1} N_a}{RT} \left( \frac{r_0^{M1}}{2} (r_0^{M1} - r_i)^2 - \frac{1}{3} (r_0^{M1} - r_i)^3 \right) \right] \quad (2)$$

563 Parabolae for 3+ ions were fitted for the M1 and M2 sites using the  
 564 REE, Ga and Al assigned to the M1 site of clinopyroxene (Fig. 8a). Fits are  
 565 weighted based on uncertainties for the element-partition coefficients. HREE  
 566 have higher element-partition coefficients than can predicted by substitution  
 567 into the M2 site, hence were fitted with ionic radii for sixfold coordination  
 568 into the M1 site (*cf.* Olin and Wolff, 2010; Reguir et al., 2012). Lattice-strain  
 569 parameters as obtained from fits to the data are shown in Table S1.

570 In some low-aegirine experiments and the Canary Islands rocks, lattice-  
571 strain fitting for 3+ ions at the M1 site was not possible, because too few  
572 HREE partitioned onto the M1 site of these clinopyroxene. Here, we chose  
573 to fit only lattice-strain parameters for the M2 site, or fix  $D_0^{3+}$  values for the  
574 M1 site to match those for the M2 site, and fit only the  $r_0$  and  $E_s$  parameters  
575 for the M1 site. Fitting of element-partitioning data for 1+, 2+ and 4+ ions  
576 was less successful owing to sparse coverage of suitable radii and detection-  
577 limit issues for some elements. Partition coefficients for 1+, 2+, and 4+  
578 elements follow radius- and charge-dependent trends consistent with lattice-  
579 strain theory and reported effects of charge on lattice-strain parameters (Fig.  
580 8b, e.g., Hazen and Finger, 1979; Law et al., 2000; Adam and Green, 2006).

581 *5.5.1. Effects of composition on ideal site size,  $r_0$*

582 As the composition of clinopyroxene shifts from augite toward aegirine,  
583 the size of the M1 and M2 sites, or strain-free radii ( $r_0$ ), should diverge fol-  
584 lowing the sizes of the major-element cations on these sites. Lattice-strain fits  
585 for 3+ cations indicate expansion of the M2 site between low and medium-  
586 aegirine clinopyroxene, with  $r_{0M2}^{3+}$  correlating well with Na replacing Ca (Figs.  
587 8, 9). Expansion of the M2 site stalls at  $r_{0M2}^{3+} \approx 1.12$  Å and  $X_{Na}^{M2} \approx 0.4$ ,  
588 changing little in size between medium and high-aegirine clinopyroxene. We  
589 suggest that this is a ‘saturation effect’, whereby the smaller ions in the T  
590 and M1 sites prevent further expansion of the M2 site as additional  $R_{M2}^{3+}$   
591 is added to the clinopyroxene. For the M1 site of clinopyroxene, strain free  
592 radii for  $R^{3+}$  cations indicate expansion between low and medium-aegirine  
593 clinopyroxene and contraction between medium and high-aegirine clinopy-  
594 roxene (Figs. 8, 9). These trends broadly follow the substitution of  $Mg^{2+}$  for

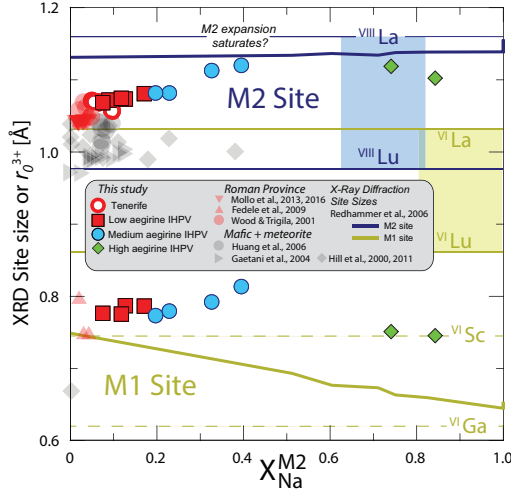


Figure 9: Diagram showing variation of ideal ionic radius  $r_0^{3+}$  with  $X_{\text{Na}}^{M2}$  for M1 and M2 sites of clinopyroxene. Shown for comparison are single crystal x-ray diffraction data from the hedenbergite-aegirine compositional join (heavy solid lines, from Redhammer et al., 2006). Shaded boxes represent the range of ionic radii for rare earth elements in VI and VIII coordination (Shannon, 1976). Literature data for the Roman Province, Italy are from Fedele et al. (2009); Mollo et al. (2013, 2016); Wood and Trigila (2001) and for mafic systems are from Hill et al. (2000, 2011); Gaetani (2004); Huang et al. (2006).

595 Fe<sup>2+</sup>, then Fe<sup>2+</sup> for Fe<sup>3+</sup> with increasing aegirine content in the clinopyrox-  
596 ene.

### 597 5.5.2. The effect of cation charge on the $D_0$ parameter

598 The  $D_0$  parameter of the lattice-strain model describes ideal, strain-free  
599 partitioning and tracks the solubility of an ideal cation in the mineral with  
600 changing pressure, temperature and the bulk composition of the system  
601 (Wood and Blundy, 2014).  $D_0$  therefore correlates with the major-element  
602 composition of the clinopyroxene. Moreover, incorporation of trace-elements

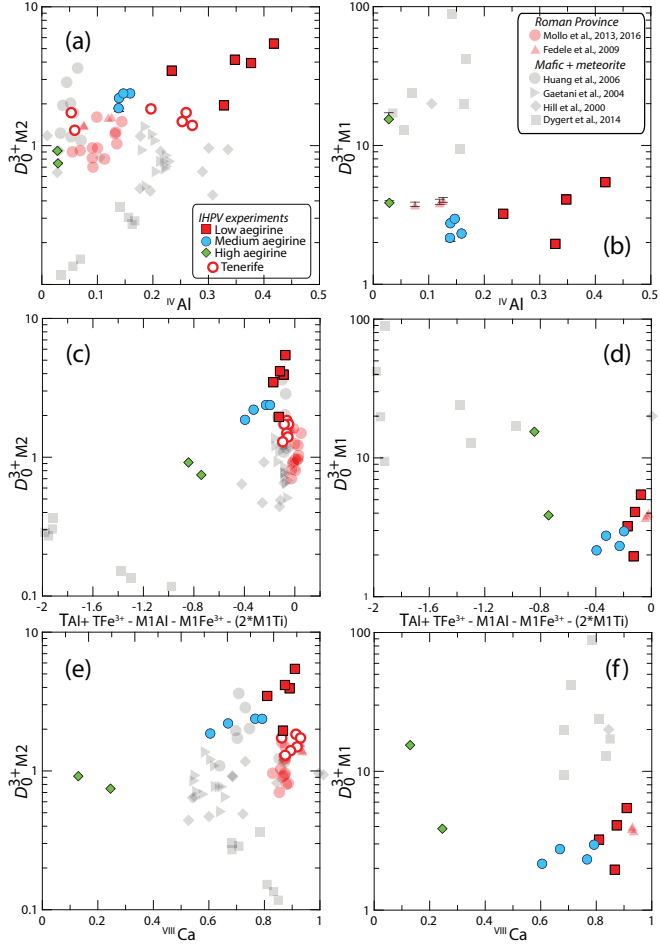


Figure 10: Strain-free partitioning coefficients ( $D_0$ ) for 3+ ions into clinopyroxene vs. various charge compensation mechanisms. (a,c,e) are for the M2 site, and (b,d,f) are for the M1 site. The diagrams show that variability in partitioning behaviour is highly dependent on mineral composition, and that variation between aegirine-rich clinopyroxene cannot be explained well by the same mechanisms as more mafic systems. Literature data for element-partitioning in Mafic + Meteorite and Roman Province compositions are from the compilation of Bédard (2014).  $1\sigma$  uncertainties are shown in (a, b) and are usually smaller than the symbol sizes.

603 of a different charge introduces an electrostatic penalty that leads to a lower  
604  $D_0$  for that charge (Wood and Blundy, 2001, 2003).

605 The average charge of major-elements on the M2 site of clinopyroxene  
606 decreases from 2+ to 1+ on the compositional join between Ca-rich diopside  
607 and Na-rich aegirine. Consequently, the electrostatic penalty for substituting  
608 a REE<sup>3+</sup> cation into the clinopyroxene M2 site is increased. Indeed,  $D_{0,M2}^{3+}$   
609 decreases as Ca exchanges for Na (Fig. 10e). Conversely, as the average  
610 charge on the M1 site of clinopyroxene increases from 2+ toward 3+ in end-  
611 member aegirine, the electrostatic penalty incurred when substituting REE<sup>3+</sup>  
612 cations onto the M1 site is reduced (Fig. 10f). As a result,  $D_{0,M1}^{3+}$  increases  
613 by approximately an order of magnitude between our medium-aegirine and  
614 high-aegirine experimental clinopyroxene, an effect that when combined with  
615 the shrinking M1 site size, leads to strong fractionation of the HREE (Figs.  
616 8 and 10f).

617 A positive correlation between Al<sup>T</sup> and partition coefficients for highly  
618 charged trace-elements has been extensively documented in studies on clinopy-  
619 roxene (Lundstrom et al., 1994; Gaetani and Grove, 1995; Blundy et al., 1998;  
620 Francis and Minarik, 2008; Hill et al., 2011; Mollo et al., 2016). The low-  
621 aegirine experimental clinopyroxene and most of the Canary Islands rocks ex-  
622 tend trends defined by clinopyroxene from mafic systems (Fig. 10a), whereas  
623 the remainder of the experimental data set and Canary Islands rocks show  
624 element-partitioning behaviour similar to the potassic Roman Province of  
625 Italy (Wood and Trigila, 2001; Fedele et al., 2009; Mollo et al., 2016), con-  
626 firming that an Al<sup>T</sup>-controlled substitution mechanism extends to peralkaline  
627 conditions (Figs. 7, 10a).

628        Tetrahedral Al is thought to facilitate incorporation of REE<sup>3+</sup> cations  
629        onto the M2 site of clinopyroxene by replacing Si<sup>4+</sup>, thereby reducing local  
630        charge and thus the electrostatic penalty associated with incorporation of  
631        REE (Blundy et al., 1998). The substitution of Fe<sup>3+</sup> for tetrahedral Si<sup>4+</sup> can  
632        be expected to have a similar effect. Conversely, R<sup>3+</sup> ions on the neighbouring  
633        M1 site should hinder incorporation of REE on the M2 site, because they  
634        increase local charge by replacing R<sup>2+</sup> ions, such as Mg<sup>2+</sup> and Fe<sup>2+</sup>. This  
635        electrostatic penalty should apply doubly to Ti<sup>4+</sup> on the M1 site. This effect  
636        is consistent with our experimental data (Fig. 10c), but is not obvious in the  
637        natural samples, nor in the majority of the literature experimental data. It  
638        would thus appear that other factors, such as melt structure, have a stronger  
639        control on  $D_{REE}$  (e.g. Prowatke and Klemme, 2005).

640         $D_0^{3+}$  parameters for the M1 site are strongly correlated with those for the  
641        M2 site, except at aegirine concentrations exceeding 50 mol.%. Similarities to  
642        M2 partitioning behaviour likely reflect the dominance of T-site substitution  
643        mechanisms in augite clinopyroxene. In the high-aegirine clinopyroxene, T-  
644        site substitutions become less important as the T-sites become saturated with  
645        Si<sup>4+</sup> (Fig. 5). The replacement of Fe<sup>3+</sup> at the M1 site by 3+ trace-elements  
646        does introduce a charge penalty, therefore  $D_{0M1}^{3+}$  increases accordingly.

647        *5.6. The effects of melt structure on element-partitioning*

648        The partitioning of trace-elements between crystals and melts is con-  
649        trolled by their relative activity in each phase and the exchange mechanisms  
650        by which their incorporation into crystals takes place (e.g., Jd-melt, Jd-DiHd  
651        and CaTS-DiHd exchanges have been shown to control REE incorporation  
652        in cpx, Putirka, 2008; Wood and Blundy, 2014; Mollo et al., 2017). As such,

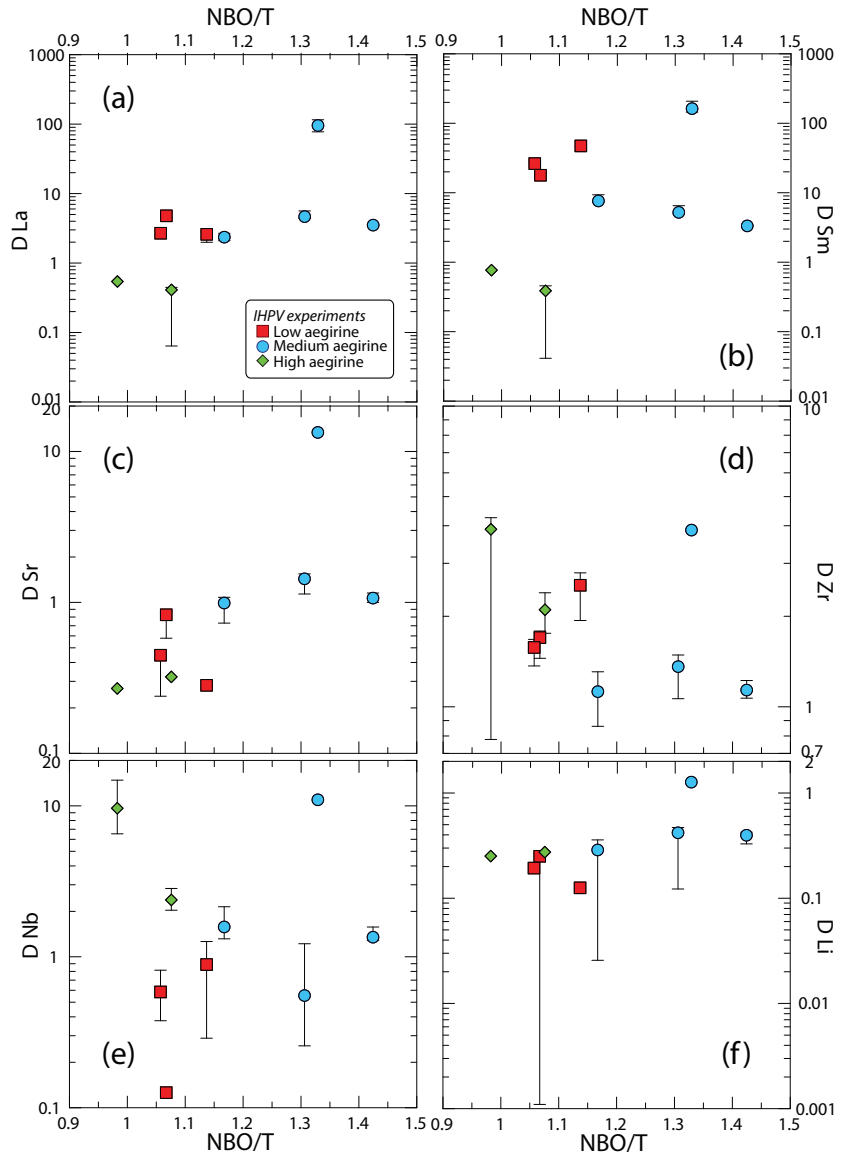


Figure 11: Diagrams of clinopyroxene–melt trace-element-partition coefficients for the IHPV experiments as a function of NBO/T of the quenched melt (Mysen et al., 1985). The water-saturated, sodic compositions investigated produce melts with highly depolymerised structures. The NBO/T ratio of these melts is not correlated with trace-element-partition coefficients, except weakly in the case of Sr. In highly polymerised systems ( $\text{NBO}/\text{T} < 0.49$ , Gaetani 2004) partition coefficients for REE and HFSE are negatively correlated with this parameter. (see Fig. 9 from Huang<sup>37</sup> et al. 2006).

one might expect to see correlations between melt structural parameters and trace-element-partition coefficients. Such correlations have been reported by numerous authors (e.g., Schmidt et al., 2006; Mollo et al., 2017), but appear to be expressed over a limited range of melt compositions (Gaetani, 2004; Huang et al., 2006). A widely used descriptor for melt structure is the ratio of non-bonding oxygen anions to tetrahedrally-coordinated cations ( $\frac{NBO}{T}$ , Mysen et al., 1982, 1985). In relatively polymerised melts, where this ratio falls below 0.49, melt structure has been shown to have a significant influence on mineral–melt partition coefficients (Gaetani, 2004; Huang et al., 2006).

To calculate NBO/T for our experiments, we estimated melt Fe oxidation state from run temperatures and known  $fO_2$  buffer conditions (Kress and Carmichael, 1991). The recalculated total of major-element oxides (incl.  $Fe_2O_3$ ) was then used to approximate the water content of the quenched melts. Oxygen from this dissolved water was added into the NBO/T calculation, which followed Mysen et al. (1985). The high content of alkalies and dissolved water in the experiments presented here produced melts that have  $NBO/T = 0.98\text{--}1.42$ ; well above the compositional boundary reported by Gaetani (2004). Consistent with his findings, most trace-element-partition coefficients determined from our experiments are uncorrelated with the NBO/T ratio of the melt (Fig. 11). An exception is  $D_{Sr}$  that shows a weak positive correlation with NBO/T (Fig. 11c). NBO/T could not be calculate for our Canary Islands compositions because the water content of the melt prior to quench is not known.

Because partition coefficients between clinopyroxene and melt are controlled by the relative activity of elements in each of these two phases, an

678 empirical model to predict partition coefficients from both melt and mineral  
679 compositional terms has the highest potential for accuracy. Application of  
680 such a model would however require measurement of both mineral and melt  
681 phases, which would limit its geological utility. A similar model based only  
682 on clinopyroxene composition could be applied in a wider range of scenarios  
683 where melt composition cannot be directly measured, for example to cumu-  
684 late systems or to concentrically zoned phenocrysts. Because crystallisation  
685 is a thermodynamically controlled process, the composition of the melt and  
686 thus its effects on element-partitioning will, at least in part, be recorded by  
687 the composition of the clinopyroxene. This considered, we chose to calibrate  
688 a clinopyroxene-based empirical partitioning model, based on lattice-strain  
689 theory that would be applicable over a wide compositional range from tholei-  
690 itic basalts to peralkaline phonolites. Details are provided in the following  
691 sections.

692 *5.7. An element-partitioning model extending to aegirine clinopyroxene*

693 Element partition coefficients vary systematically with the physiochemi-  
694 cal conditions of natural and synthetic magmas (cf. Wood and Blundy, 2003).  
695 Consequently, a host of models have been presented to describe the system-  
696 atics of element-partitioning between clinopyroxene and silicate melts (Wood  
697 and Blundy, 1997, 2001; Hill et al., 2011; Yao et al., 2012; Sun and Liang,  
698 2012; Bédard, 2014; Dygert et al., 2014; Mollo et al., 2016). The majority of  
699 these models are based on lattice-strain theory and predict how the lattice  
700 parameters  $r_0$ ,  $E_s$ , and  $D_0$  vary with composition, temperature and pressure.  
701 This semi-thermodynamic approach theoretically permits calculation of par-  
702 tition coefficients for any trace-element, at any set of  $P - T - X$  conditions.

703 In reality, all models have a limited working range, as restricted by the input  
704 data set. Because existing partitioning models do not reproduce the high  
705  $r_{0,M2}^{3+}$  values for clinopyroxene with aegirine contents  $\geq 50$  mol % (Fig. 12a),  
706 they cannot accurately predict REE partitioning behaviour for strongly per-  
707 alkaline systems. Here, we present a new empirical model that is calibrated  
708 on both our experimental work and natural partition coefficients from Ca-  
709 nary Islands rocks, as well as existing partitioning data from the literature  
710 (compilation of Bédard, 2014, Fig. 12, Table S1).

711 Our model focuses on the dependence of element-partitioning on clinopy-  
712 roxene composition, temperature and pressure only. While partition coeffi-  
713 cients are thermodynamically controlled by activity of elements in both the  
714 crystal and the melt phase (Wood and Blundy, 2014), and while melt struc-  
715 ture has been shown to influence element-partitioning (Huang et al., 2006;  
716 Schmidt et al., 2006; Mollo et al., 2017), it is not always possible to measure  
717 melt composition directly. For example, equilibrium melt compositions can-  
718 not be measured for the cores of zoned clinopyroxene phenocrysts in tephra,  
719 or indeed for any crystal from an intrusion in which gravitational segregat-  
720 tion of phases has occurred. Therefore, while the predictive power of a model  
721 based only on the compositions of the crystal should be lower than that of  
722 a model based on both crystal and melt compositions, a crystal-only model  
723 may be applied to a wider spectrum of geological scenarios. Melt composi-  
724 tion should, at least in part, be recorded by the major-element composition  
725 of the clinopyroxene.

726 5.7.1. *The clinopyroxene M2 site*

727 To find the principal physiochemical factors that affect element-partitioning  
728 at the M2 site of clinopyroxene, a stepwise least-squares multiple linear re-  
729 gression analysis was performed using the lattice-strain parameters  $r_0^{3+}$ ,  $E_s^{3+}$   
730 and  $D_0^{3+}$ , temperature, pressure and clinopyroxene composition as inputs.  
731 Input parameters were initially examined in binary scatter diagrams to as-  
732 certain whether correlations with lattice-strain parameters were linear. If  
733 not, interaction compositional terms were added to the initial set of possible  
734 fitting parameters that had linear correlations with lattice-strain parameters  
735 (e.g.  $X_{Al+Fe^{3+}}^T$ ). Intensive variables for multiple regression models for  $r_0$ ,  
736  $E_s$  and  $D_0$  were introduced following a hierarchical forward selection crite-  
737 rion with switching. The largest number of significant terms to describe a  
738 lattice-strain parameter was eight for  $E^{M2}$  (c.95%, cf. Supplement S4).

739 Because of systematic covariation of compositional parameters in our  
740 small data set of experiments and natural samples ( $n = 16$ ), a model cal-  
741 ibrated with these points alone would be unable to deconvolve the effects  
742 of each major-element on partitioning behaviour. We have therefore added  
743 published experiments and natural phenocryst-glass pairs ( $n = 75$ ) to assem-  
744 ble a database covering a wide range of composition, pressure, temperature  
745 and oxygen fugacity (data from compilation of Bédard 2014, and Mollo et al.  
746 2016, 0.0001–3.5 GPa, 650–1345 °C,  $\log fO_2 = IW$  to  $MH \approx \Delta QFM -5$   
747 to +5). clinopyroxene compositions cover  $X_{Mg}$  0.031–1,  $X_{Na}^{M2}$  0–0.84 and  
748  $Al^T$  0–0.49 c.f.u. and melt compositions vary widely in terms of Mg# (0–  
749 100) and  $X_{H_2O}$  (0–0.38). REE partition coefficients also vary significantly  
750 (e.g.  $D_{La}$  0.01–4.79;  $D_{Sm}$  0.02–47.24, and  $D_{Yb}$  0.11–8.00). The majority

751 of partition coefficients in the training data set were measured via SIMS  
 752 or LA-ICP-MS, minimising analytical uncertainty (e.g. from analyses by  
 753 electron-microprobe).

754 The resultant empirical model accounts well for changes in lattice-strain  
 755 parameters over a range of compositions from basalt to peralkaline phono-  
 756 lite, faithfully reproducing large  $r_0^{M2}$  values typical for sodic clinopyroxene  
 757 (Fig. 12, model coefficients in Table 5). Student t-tests show that all of the  
 758 independent variables included in the models are significant at the 95% con-  
 759 fidence level and PRESS  $R^2$  values were obtained by repeatedby randomly  
 760 subsampling the dataset (Stevens, 1996), are close to  $R^2$  values calculated by  
 761 regular methods, indicating robust models with high predictive power. Full  
 762 multiple regression reports are available in Supplement S4. Equations gen-  
 763 erated by the multiple linear regression calculations are given below for the  
 764 M2 site, where  $a_i$  are the regression coefficients for the respective variables:  
 765

$$\ln D_0^{M2} = a_1 + a_2 T + a_3 X_{Al+Fe^{3+}}^T + a_4 X_{Ti}^{M1} + a_5 X_{Al-Fe^{3+}}^{M1} + a_6 X_{Fe^{2+}}^{M2} \quad (3)$$

$$E^{M2} = a_7 + a_8 P + a_9 X_{Al+Fe^{3+}}^T + a_{10} X_{Al}^{M1} + a_{11} X_{Mg}^{M1} + a_{12} X_{Ti}^{M1} \quad (4) \\ + a_{13} X_{Mg}^{M2} + a_{14} X_{Mg}$$

$$r_0^{M2} = a_{15} + a_{16} T + a_{17} X_{Al-Fe^{3+}}^{M1} + a_{18} X_{Ti}^{M1} + a_{19} X_{Ca}^{M2} + a_{20} X_{Na}^{M2} \quad (5)$$

766 The model for  $r_0^{M2}$  is robust with high predictive power and incorporates  
 767 compositional controls from the M1 and M2 sites, as well as temperature.

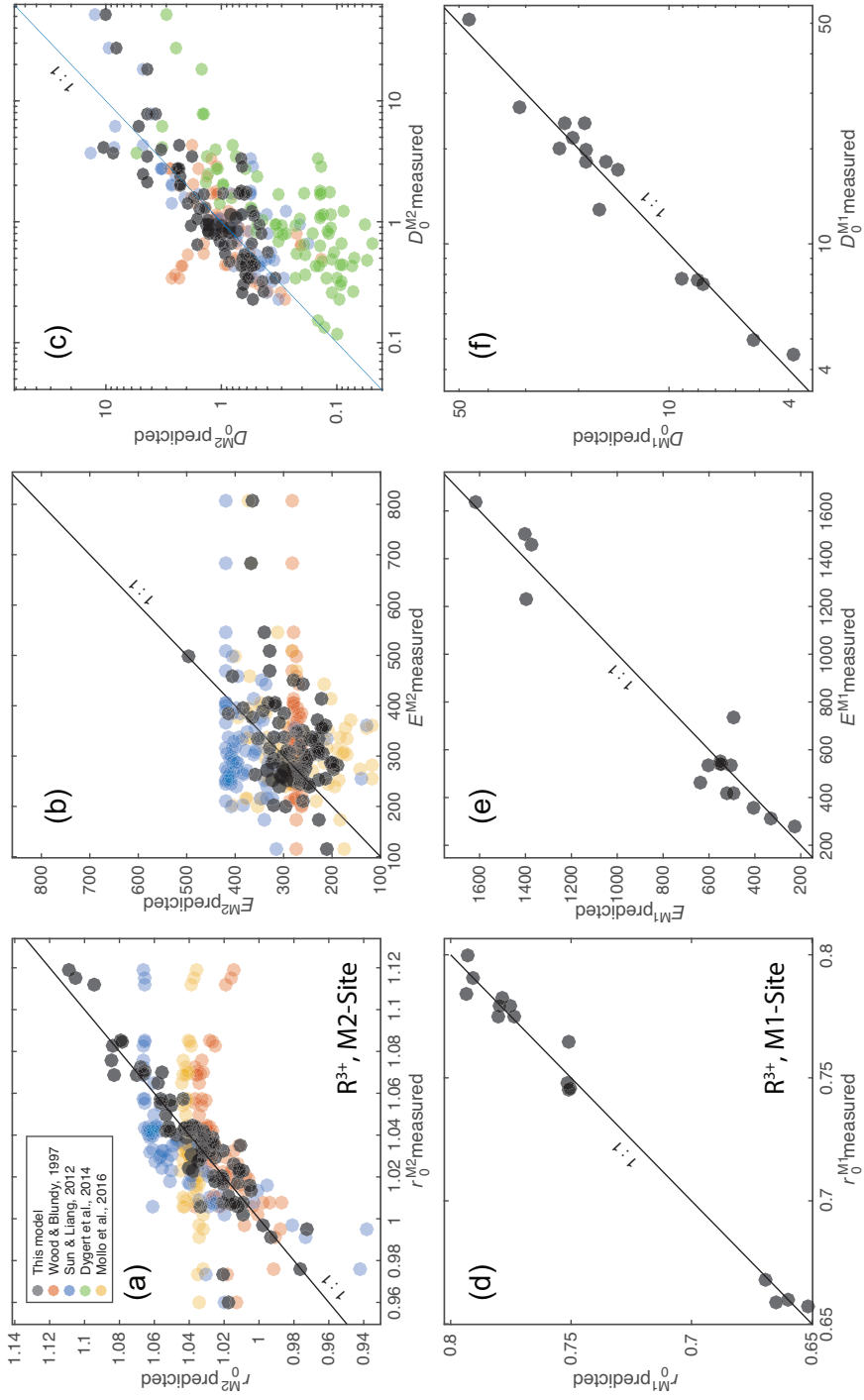


Figure 12: Measured vs. predicted model values for lattice-strain parameters for the M2 and M1 sites of clinopyroxene. The new models presented here were generated via a stepwise multiple linear regression procedure following a hierarchical forward selection criterion with switching. Full regression reports are in Supplement S4 and model equations are in the main text.

768 Elevated concentrations of large M2 cations  $\text{Ca}^{2+}$  and  $\text{Na}^+$  are correlated  
769 with large M2 sites.  $\text{Ti}^{4+}$  cations in the neighbouring M1 site are also cor-  
770 related with expansion of the M2 site, and the concentration of small  $\text{Al}^{3+}$   
771 minus larger  $\text{Fe}^{3+}$  on the M1 site is negatively correlated with  $r_0^{M2}$ . The neg-  
772 ative correlation between  $r_0^{M2}$  and temperature reflects the sum of changes  
773 to major-element composition that lead to smaller clinopyroxene M2 sites at  
774 higher temperatures. This compositional effect swamps the minor influence  
775 of thermal expansion.

776  $D_0^{M2}$  is reasonably well predicted and incorporates compositional terms  
777 from all three sites in clinopyroxene and temperature. The positive effect  
778 of tetrahedral  $\text{R}^{3+}$  on  $D_0^{M2}$  is the largest contribution to the model, which  
779 is consistent with published studies (see above). The relationship between  
780 clinopyroxene compositional terms on the M1 and M2 sites and  $D_0$  are in-  
781 direct and are tied to the solubility of the mineral in the melt (Wood and  
782 Blundy, 2003), which in turn is tied to the physiochemical conditions of the  
783 system (largely melt composition). The model for  $D_0^{M2}$  is less robust than  
784 that for  $r_0^{M2}$ , largely because there are melt compositional effects that are  
785 not recorded in the composition of the clinopyroxene. We tested the Mg#  
786 and  $X\text{H}_2\text{O}$  of the melt, neither of which are significant predictors for  $D_0^{M2}$ .

787 The model for  $E^{M2}$  is less well-constrained than for the other two M2  
788 lattice-strain parameters, suggesting that M2 site stiffness is not tied strongly  
789 to clinopyroxene composition, temperature or pressure. Despite a signifi-  
790 cantly lower predictive power, this model still has physical grounding. Stiff-  
791 ness of the M2 site is positively correlated with pressure, as might be expected  
792 following a simple Hooke's law relationship, and there are some subtle com-

793 positional controls imparted by the T and M1 sites. The poor correlation  
794 between  $E^{M2}$ , clinopyroxene composition, temperature and pressure is also  
795 evident in published element-partitioning models, where  $E^{M2}$  is either poorly  
796 predicted (Fig. 12b), or set to a fixed value (e.g. Dygert et al., 2014).

797 Diagrams of measured vs. predicted D values for R<sup>3+</sup> cations are given in  
798 Figure 13a, showing the predictive power of the models over a compositional  
799 range between basalt and peralkaline phonolite. For the M2 site, 95% of  
800 the measured R<sup>3+</sup> partition coefficients are reproduced within a factor of  
801  $\pm 2.5$  (hard dashed lines), and in extreme cases, the model still reproduces D  
802 values within an order of magnitude, sufficient for the prediction of element-  
803 partitioning trends over a wide range of  $P - T - X$ .  $D_{MREE}$ , such as Sm,  
804 are reproduced more faithfully than  $D_{LREE}$ , because their radius is closer to  
805  $r_0^{M2}$  (Fig. 13c,d), and therefore prediction of their partitioning behaviour is  
806 affected less strongly by inaccuracies in predicted  $E^{M2}$  values.

807 *5.7.2. The clinopyroxene M1 site*

808 Using a methodology similar to the M2 site, we fitted a predictive model  
809 for partitioning of R<sup>3+</sup> cations onto the smaller, 6-coordinated M1 site of  
810 clinopyroxene. Lattice-strain parabola were constrained by partitioning data  
811 for Cr, Ga, Sc, and where suitable, the HREE Tm, Yb and Lu (Our IHPV  
812 experiments plus Hill et al. 2000; Fedele et al. 2009; Mollo et al. 2013; Dygert  
813 et al. 2014). The training data set for the M1 site partitioning model is  
814 small relative to that for the M2 site ( $n = 18$ ), and because it is strongly  
815 skewed toward alkaline compositions, it has lower predictive power and is  
816 not recommended for application to mafic magmatic systems. Equations for  
817 the M1 site lattice-strain parameters, as generated by multiple linear least

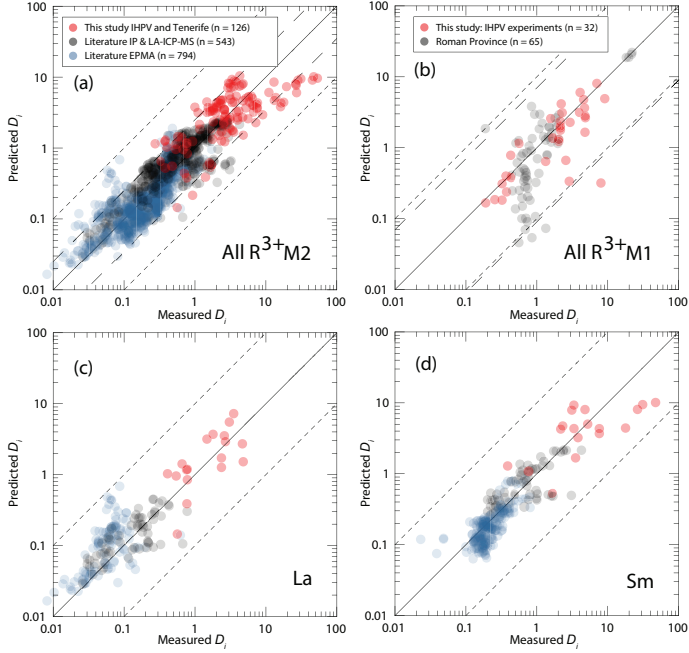


Figure 13: Measured clinopyroxene–silicate melt partition coefficients for 3+ cations vs. those predicted by our empirical model. (a) shows a comparison between measured partition coefficients and model-derived values for the M2 site of clinopyroxene. Hard dashed lines represent 95% confidence intervals of the model, and correspond to maximum uncertainties of factor  $\frac{+2.5}{-2.9}$ . Fine dashed lines represent 1 order of magnitude uncertainty (extreme outliers for M2 model). Partition coefficients in this diagram are the REE La to Er for our IHPV experiments, Canary Islands rocks, and literature data from the Roman Province (Wood and Trigila, 2001; Fedele et al., 2009; Mollo et al., 2013, 2016), and all the REE plus Y for the rest of the data compilation (Bédard, 2014), which is split by analytical methodology. (b) shows performance of the predictive model for the M1 site that is calibrated for alkaline magmatic systems, and includes data from our IHPV experiments and the Roman Province (Fedele et al., 2009; Mollo et al., 2013, 2016). Maximum uncertainties at the 95% confidence interval are a factor of  $\frac{+7}{-11}$ , higher than for the M2 site because of the smaller calibrating data set. (c) performance of the M2 site model for La, and (d) for Sm.

818 squares regression, are given below and shown in Figure 12 where  $b_i$  are the  
 819 regression coefficients (Table 5) for the respective variables:

$$\ln D_0^{M1} = b_1 + b_2 X_{Al}^T + b_3 X_{Fe^{2+}}^{M1} + b_4 X_{Ca}^{M2} + b_5 X_{Na}^{M2} \quad (6)$$

$$E^{M1} = b_6 + b_7 T + b_8 P + b_9 X_{Mg}^{M1} \quad (7)$$

$$r_0^{M1} = b_{10} + b_{11} P + b_{12} X_{Mg}^{M2} + b_{13} X_{Fe^{3+}}^{M1} + b_{14} X_{Ca}^{M2} \quad (8)$$

820 The model for  $r_0^{M1}$  is robust and accurately reproduces the input data  
 821 set. A negative pressure term may reflect compressional strain on the crystal  
 822 lattice. Large Fe<sup>3+</sup> cations have a positive effect on the size of the M1 site,  
 823 while smaller Mg<sup>2+</sup> cations on the neighbouring M2 site have a negative effect  
 824 on M1 site size. The small negative  $X_{Ca}^{M2}$  term is indirectly related to the  
 825 size of the M1 site.

826  $E^{M1}$  is predicted more accurately than  $E^{M2}$  and is largely described by  
 827 variations in temperature and pressure. Much like the M2 site, stiffness of  
 828 the M1 site appears to be controlled dominantly by physicochemical factors  
 829 that are not recorded in the composition of the clinopyroxene.

830 The model for  $D_0^{M1}$  contains compositional terms from all three crystal-  
 831 lographic sites in clinopyroxene.  $X_{Al}^T$  has a strong positive correlation with  
 832  $D_0^{M1}$ , consistent with a charge compensation mechanism that aids incorpora-  
 833 tion of R<sup>3+</sup> cations, while terms for M1 and M2 site cations may be indirectly

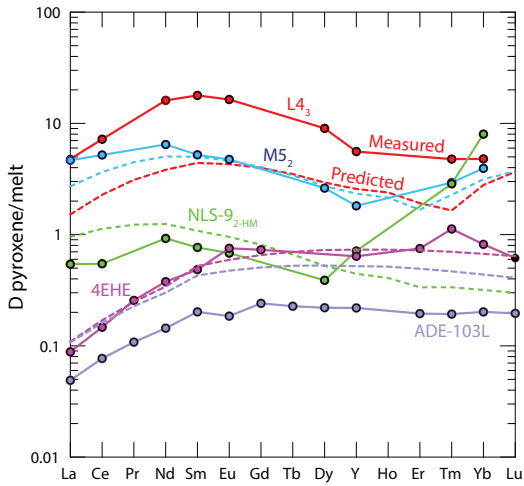


Figure 14: Measured and predicted element-partition coefficients for  $\text{REE}^{3+}$ . The model does not introduce notable radius-dependent biases, except for in our high-aegirine clinopyroxene (NLS-9<sub>2</sub>-HM in green) for which  $D_{\text{HREE}}$  are strongly underpredicted, owing to inaccurate return of  $D_0^{M1}$ . Shown for comparison are two diopside–melt pairs: 4EHE from Hill et al. (2000), grown from a synthetic (NCMAS) basaltic andesite composition and ADE-103L from Lofgren et al. (2006) grown from a picritic composition based on the Angra dos Reis meteorite.

recording melt compositional effects. Because  $D_0^{M1}$  is unusually high for our high-aegirine experiments, they had to be excluded from the fitting procedure to permit model convergence. The models for  $r_0^{M1}$  and  $E^{M1}$  are calibrated for use all the way to end-member aegirine, but this was not possible for the  $D_0^{M1}$  term, which is calibrated for use up to  $\sim\text{Ae}_{50}$ . Further experiments at conditions between those that generated our medium and high-aegirine clinopyroxene would be required to better constrain the clinopyroxene compositional record of  $D_0^{M1}$  in strongly peralkaline Fe-rich magmas.

When applied to our experimental data, and the compilation of partition coefficients from the Roman Province (Fedele et al., 2009; Mollo et al., 2013, 2016), the M1 stepwise model reproduces element-partitioning data to a factor of  $\frac{+7}{-11}$  at the 95% confidence interval (Fig. 13b). Full regression reports are provided in Supplement S4.

For convenience, we provide an EXCEL spreadsheet for calculation of clinopyroxene-melt element-partition coefficients for any trace-element of 3+ valence that is large enough to fit onto the M1 or M2 sites of clinopyroxene (Supplement S5). To assess the utility of the partitioning models and to monitor for potential introduction of radius-dependent bias, we show predicted REE patterns normalised to measured ratios for some literature data and our internally heated pressure vessel experiments (Fig. 14). The model accurately reproduces REE patterns at all compositions, except for HREE on the M1 site of clinopyroxene at aegirine contents exceeding  $\sim 50$  mol% (NLS experiments).

857    5.8. Implications for formation of REE deposits in evolved alkaline intrusions

858    The solubility of REE and HFSE minerals is strongly enhanced in peral-  
859    kaline melts (Watson, 1979; Linnen and Keppler, 1997; Boehnke et al., 2013;  
860    Aseri et al., 2015), thus the high concentration of these elements in peralka-  
861    line systems may (partially) reflect this fact (Dostal, 2017). Melts containing  
862    high concentrations of REE and HFSE are thought to be generated through  
863    low degrees of anatexis in the source, followed by residual enrichment during  
864    protracted fractional crystallisation (Marks and Markl, 2017). The budget  
865    of REE and HFSE in a fractionating magma is influenced by the mineralogy  
866    of the crystallising assemblage, and the extent to which these elements are  
867    incorporated at minor or trace concentrations.

868    Pyroxene is a major ferromagnesian phase that is commonly saturated  
869    throughout the entire differentiation histories of peralkaline magmatic sys-  
870    tems (Ablay et al., 1998; Marks and Markl, 2001; Möller and Williams-Jones,  
871    2016). The composition of the fractionating clinopyroxene has a major im-  
872    pact on the absolute REE concentrations and REE pattern of the resid-  
873    ual melt, and ultimately on the ability of a system to develop economic  
874    concentrations of the REE (Fig. 15, e.g. Kogarko, 1990; Sørensen, 1992;  
875    Marks et al., 2011). Pyroxene in alkaline magmatic systems is initially cal-  
876    cic for mafic melts, and becomes increasingly sodic as crystal fractionation  
877    proceeds (Marks et al., 2004). Although the REE are compatible in the  
878    majority of our experimentally generated clinopyroxene, those approaching  
879    aegirine end-member composition, as found in evolved alkaline magmatic  
880    systems have the lowest  $D_{REE}$  values (Fig. 6). Strongly alkaline magmatic  
881    systems are thought to crystallise abundant Ca-pyroxene early in their evolu-

tion which may deplete residual liquids with respect to REEs. Consequently, even though crystallisation of Na-pyroxene could enrich residual liquids with REE, the resultant concentration of these metals in the melt would remain low. However, clinopyroxene is not the only phase to crystallise from alkaline magmas, and the majority of additional silicate phases, such as olivine, biotite and feldspar have  $D_{REE} \ll 1$ , typically 1-4 orders of magnitude lower than clinopyroxene (Larsen, 1979; Kovalenko et al., 1988; Mahood and Stimac, 1990). Consequently, if the mode of clinopyroxene is low enough, the bulk  $D_{REE}$  of the crystallising assemblage would remain below unity, allowing the REE to become enriched in the residual silicate melt.

To give insight into the optimum conditions for residual magmatic enrichment of the REE in alkaline systems we modelled the evolution of REE concentrations in the melt during fractional crystallisation of a nepheline syenite body (Fig. 15). Phase relation data and clinopyroxene compositions are from the experimental study of Giehl et al. (2013). Their starting composition, based on the MiKa dyke, from the Gardar Province, Greenland, is already extremely evolved, with  $Mg\# = 2$ ,  $(Na + K)/Al = 1.44$  and  $FeO^* = 12$  wt.%.

In these models, crystallisation under water-bearing, oxidising conditions produces a high fraction of clinopyroxene that depletes residual melts with respect to Sm, while subtly enriching La. Dry conditions promote abundant alkali feldspar (Afs) crystallisation, which effectively enriches the REE content of residual melts. Under oxidising, dry conditions, the La/Sm ratio of the residual melt increases with fractionation, because Sm is more effectively incorporated into clinopyroxene. Residual enrichment is most ef-

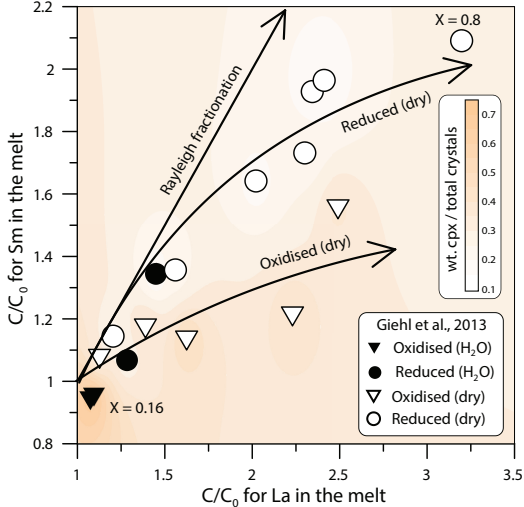


Figure 15: Model enrichment paths for La and Sm in residual melts during fractional crystallisation of a MiKa dyke composition (Gardar Province, Greenland, see Marks and Markl 2003). Phase relations and clinopyroxene compositions are from Giehl et al. (2013) and pertain to both oxidising and reducing conditions ( $\log f\text{O}_2 = \Delta\text{QFM} -3$  and +1), nominally dry to water bearing (to 3 wt.%  $\text{H}_2\text{O}$  at 1 kbar). Colour shading indicates the weight fraction of clinopyroxene within the crystallising assemblage. Bold arrows indicate residual enrichment pathways for the REE in the melt for Rayleigh fractionation (no incorporation into crystals), reduced, dry conditions, and oxidised dry conditions (the latter two are hand drawn fits to the data). For simplicity, this model does not consider REE incorporation into magnetite, alkali-feldspar, olivine, nepheline or aenigmatite, all phases generated in the experiments of Giehl et al. (2013) (see Larsen, 1979; Kovalenko et al., 1988; Mahood and Stimac, 1990).

907 effective under dry, reducing conditions because of a relatively lower fraction  
 908 of clinopyroxene within the crystallising assemblage. Because of this, the  
 909 REE enrichment path of the residual melt is close to that of ideal Rayleigh  
 910 fractionation. Under these reducing, dry conditions and at a temperature of

911 750°C, the experiments of Giehl et al. (2013) attained a crystal fraction of  
912 0.8. Here, residual melts would have and 3.2 times La concentration and 2  
913 times the Sm concentration relative to their starting composition.

914 Considering these mechanisms, alongside our experimental and Canary  
915 Islands data, the best systems to develop high REE concentrations are those  
916 that would produce small proportions of Ca-pyroxene early in their crystalli-  
917 sation histories, quickly evolving to more sodic compositions that crystallise  
918 aegirine clinopyroxene. Cooling under low-pressure, dry, reducing conditions  
919 produces abundant alkali feldspar that in the case of a peralkaline compo-  
920 sition, would serve to further increase the alkalinity of the residual melt.  
921 Low degrees of source melting would produce primary melts with (1) high  
922 REE concentrations and (2) low melt Mg + Fe, and low modal abundance  
923 of clinopyroxene, which would aid enrichment in residual melts via fractional  
924 crystallisation.

925 The HREE-rich nature of peralkaline magmatic systems, both granites  
926 and nepheline syenites, is compatible with fractionation of moderately sodic  
927 clinopyroxene that have high  $D_{LREE}/D_{HREE}$  (e.g. Möller and Williams-  
928 Jones, 2016; Dostal, 2017). As crystal fractionation progresses and clinopy-  
929 roxene compositions evolve toward the aegirine end-member composition,  
930  $D_{LREE}/D_{HREE}$  decreases (Fig. 6). This systematic change in element-  
931 partitioning behaviour would result in strong HREE enrichment in aegirine-  
932 pyroxene cumulates, and would enrich the residual melt with respect to  
933 LREE-MREE.

934 **Conclusions**

- 935 • Our experiments reveal three distinct element-partitioning behaviours  
936 for Na-rich clinopyroxene that depend on aegirine content. Each of  
937 these is associated with a distinct major-element exchange vector. We  
938 do not have the compositional resolution to know if the transition be-  
939 between these behaviours is smooth or step-like.
- 940 • Fits to the lattice-strain model of Blundy and Wood (1994) indicate  
941 expansion of the M2 site with increasing  $\text{Na}_{\text{M2}}^{+}$ , to a maximum  $r_{0,\text{M2}}^{3+}$  of  
942 1.12 Å at  $\text{Na}_{\text{M2}}^{+} = 0.4$  c.f.u. Further expansion did not occur at higher  
943 Na contents.
- 944 • Both the M1 and M2 sites shrink at high-aegirine contents in response  
945 to increasing  $\sum \text{R}_{\text{M1}}^{3+}$ .
- 946 • Charge effects lead to a progressive increase in  $D_0^{M1}$  at the expense  
947 of  $D_0^{M2}$ , as the exchanges  $\text{Ca}^{2+}$  for  $\text{Na}^{+}$  and  $\text{M}^{2+}$  for  $\text{Fe}^{3+}$  take place.  
948 Much like in systems of lower alkalinity, REE incorporation into clinopy-  
949 roxene is dominated by coupled Al–Si substitutions at the T-site.
- 950 • Existing predictive models for clinopyroxene/melt element-partitioning  
951 do not accurately reproduce the large M2 site ( $r_{0,\text{M2}}^{3+}$ ) of clinopyroxene  
952 with aegirine content exceeding 50 mol%. We have calibrated a new  
953 empirical model that may be applied to any composition between basalt  
954 and peralkaline phonolite, based on our data from experiments and  
955 natural systems, as well as a large compilation of partition coefficients  
956 from the literature.

- 957     ● Crystallisation of abundant Ca-Mg rich clinopyroxene depletes the resid-  
958       ual melts of REE, and inhibits or terminates magmatic enrichment  
959       processes.
- 960     ● Element partitioning systematics suggest that nepheline syenites which  
961       host REE deposits must originate from low-degree melts with sufficient  
962       alkali enrichment to saturate clinopyroxene similar to our medium-  
963       aegirine clinopyroxene ( $Ae_{25-50}$ ). Fractionation of such clinopyroxene  
964       enriches residual melts with respect to the HREE, in accord with the  
965       composition of REE-mineralised nepheline syenite systems.

966     **Acknowledgements**

967       We thank the Geo.X partners GFZ and Universität Potsdam for ac-  
968       cess to the HP-GeoMatS Lab, Don Baker for assistance with preparation  
969       of starting materials, Bruce Watson and Volker Möller for providing sam-  
970       ples of Mud Tank zircon and the Nechalacho rocks, respectively, Hans Peter  
971       Nabein, Maria Stuff and Julia Pohlenz for assistance with HP experimen-  
972       tal equipment, Toby Soutar for help with preparation of the Canary Islands  
973       samples, Lang Shi and Glenn Poirier for assistance with electron-microprobe  
974       analyses, and Anna Jung for assistance with laser ICP-MS analyses. The  
975       manuscript benefitted from discussions with Longbo Yang, Rebecca Paisley,  
976       Shane Rooyakkers and Jean Bédard. Silvio Mollo and an anonymous re-  
977       viewer are thanked for their insightful feedback. Nelson Eby is thanked for  
978       editorial handling. This work was funded by PhD scholarships to C.B. from  
979       Geotop, DIVEX, and the SEG Canada Foundation, and operating grants to  
980       V.vH. and J.S. from the Natural Sciences and Engineering Research Coun-

981 cil of Canada (grant numbers RGPIN-2014-05955, RGPAS-462335-2014) and  
982 the FQRNT team research project program.

983 **References**

- 984 Ablay, G.J., Carroll, M.R., Palmer, M.R., Martí, J., Sparks, R.S.J.,  
985 1998. Basanite–phonolite lineages of the Teide–Pico Viejo volcanic  
986 complex, Tenerife, Canary Islands. *Journal of Petrology* 39, 905–936.  
987 doi:10.1093/petroj/39.5.905.
- 988 Ablay, G.J., Ernst, G.G.J., Marti, J., Sparks, R.S.J., 1995. The 2 ka sub-  
989 plinian eruption of Montaña Blanca, Tenerife. *Bulletin of Volcanology* 57,  
990 337–355. doi:10.1007/BF00301292.
- 991 Adam, J., Green, T., 2006. Trace element partitioning between mica- and  
992 amphibole-bearing garnet lherzolite and hydrous basanitic melt: 1. Exper-  
993 imental results and the investigation of controls on partitioning behaviour.  
994 *Contributions to Mineralogy and Petrology* 152, 1–17. doi:10.1007/s00410-  
995 006-0085-4.
- 996 Akasaka, M., Onuma, K., 1980. The join CaMgSi<sub>2</sub>O<sub>6</sub>-CaFeAlSiO<sub>6</sub>-  
997 CaTiAl<sub>2</sub>O<sub>6</sub> and its bearing on the Ti-rich fassaitic pyroxenes. *Contri-  
998 butions to Mineralogy and Petrology* 71, 301–312. doi:10.1007/BF00371672.
- 999 Albert, H., Costa, F., Martí, J., 2015. Timing of magmatic processes and  
1000 unrest associated with mafic historical monogenetic eruptions in Tenerife  
1001 Island. *Journal of Petrology* 56, 1945–1966. doi:10.1093/petrology/egv058.

- 1002 Andújar, J., Scaillet, B., 2012. Experimental constraints on parameters con-  
1003 trolling the difference in the eruptive dynamics of phonolitic magmas: the  
1004 case of Tenerife (Canary Islands). *Journal of Petrology* 53, 1777–1806.  
1005 doi:10.1093/petrology/egs033.
- 1006 Aseri, A.A., Linnen, R.L., Che, X.D., Thibault, Y., Holtz, F., 2015. Effects of  
1007 fluorine on the solubilities of Nb, Ta, Zr and Hf minerals in highly fluxed  
1008 water-saturated haplogranitic melts. *Ore Geology Reviews* 64, 736–746.  
1009 doi:10.1016/j.oregeorev.2014.02.014.
- 1010 Beard, C.D., 2018. Mineral-melt trace element partitioning in alkaline mag-  
1011 matic systems. Phd thesis. McGill University.
- 1012 Bédard, J.H., 2014. Parameterizations of calcic clinopyroxene - Melt trace  
1013 element partition coefficients. *Geochemistry, Geophysics, Geosystems* 15,  
1014 303–336. doi:10.1002/2013GC005112.
- 1015 Behrens, H., Hahn, M., 2009. Trace element diffusion and viscous flow in  
1016 potassium-rich trachytic and phonolitic melts. *Chemical Geology* 259, 63–  
1017 77. doi:10.1016/j.chemgeo.2008.10.014.
- 1018 Berndt, J., Liebske, C., Holtz, F., Freise, M., Nowak, M., Ziegenbein,  
1019 D., Hurkuck, W., Koepke, J., 2002. A combined rapid-quench and H<sub>2</sub>-  
1020 membrane setup for internally heated pressure vessels: description and  
1021 application for water solubility in basaltic melts. *American Mineralogist*  
1022 87, 1717–1726. doi:10.1029/JB089iB10p08540.
- 1023 Blundy, J., Wood, B., 1994. Prediction of crystal–melt partition coefficients  
1024 from elastic moduli. *Nature* 372, 452–454. doi:10.1038/372452a0.

- 1025 Blundy, J.D., Robinson, J.A.C., Wood, B.J., 1998. Heavy REE are compat-  
1026 ible in clinopyroxene on the spinel lherzolite solidus. *Earth and Planetary*  
1027 *Science Letters* 160, 493–504. doi:10.1016/S0012-821X(98)00106-X.
- 1028 Bohnke, P., Watson, E.B., Trail, D., Harrison, T.M., Schmitt, A.K.,  
1029 2013. Zircon saturation re-revisited. *Chemical Geology* 351, 324–334.  
1030 doi:10.1016/j.chemgeo.2013.05.028.
- 1031 Borchert, M., Wilke, M., Schmidt, C., Cauzid, J., Tucoulou, R., 2010. Par-  
1032 titioning of Ba, La, Yb and Y between haplogranitic melts and aque-  
1033 ous solutions: An experimental study. *Chemical Geology* 276, 225–240.  
1034 doi:10.1016/j.chemgeo.2010.06.009.
- 1035 Boudreau, A.E., 2004. PALLADIUM, a program to model the chromato-  
1036 graphic separation of the platinum-group elements, base metals and sulfur  
1037 in a solidifying pile of igneous crystals. *Canadian Mineralogist* 42, 393–403.  
1038 doi:10.2113/gscanmin.42.2.393.
- 1039 Brown, R.J., Barry, T.L., Branney, M.J., Pringle, M.S., Bryan, S.E., 2003.  
1040 The Quaternary pyroclastic succession of southeast Tenerife, Canary Is-  
1041 lands: explosive eruptions, related caldera subsidence, and sector collapse.  
1042 *Geological Magazine* 140, 265–288. doi:10.1017/S0016756802007252.
- 1043 Bryan, S.E., Martí, J., Cas, R.A.F., 1998. Stratigraphy of the Bandas del  
1044 Sur Formation: an extracaldera record of Quaternary phonolitic explo-  
1045 sive eruptions from the Las Cañadas edifice, Tenerife (Canary Islands).  
1046 *Geological Magazine* 135, 605–636. doi:null.

- 1047 Carracedo, J.C., Badiola, E.R., Guillou, H., Paterne, M., Scaillet, S.,  
1048 Torrado, F.J.P., Paris, R., Fra-Paleo, U., Hansen, A., 2007. Eruptive  
1049 and structural history of Teide Volcano and rift zones of Tenerife, Ca-  
1050 nary Islands. Geological Society of America Bulletin 119, 1027–1051.  
1051 doi:10.1130/B26087.1.
- 1052 Carroll, M.R., Blank, J.G., 1997. The solubility of H<sub>2</sub>O in phonolitic melts.  
1053 American Mineralogist 82, 549–556. doi:10.1093/petrology/32.5.1021.
- 1054 Chou, I.M., 1986. Permeability of precious metals to hydrogen at 2 kb total  
1055 pressure and elevated temperatures. American Journal of Science 286,  
1056 638–658.
- 1057 Corgne, A., Wood, B.J., 2005. Trace element partitioning and substitu-  
1058 tion mechanisms in calcium perovskites. Contributions to Mineralogy and  
1059 Petrology 149, 85–97. doi:10.1007/s00410-004-0638-3.
- 1060 Costa, F., Chakraborty, S., Dohmen, R., 2003. Diffusion coupling between  
1061 major and trace elements and a model for the calculation of magma cham-  
1062 ber residence times using plagioclase. Geochimica et Cosmochimica Acta  
1063 67, 2189–2200. doi:10.1016/S0016-7037(00)01345-5.
- 1064 Coumans, J.P., Stix, J., Clague, D.A., Minarik, W.G., Layne, G.D., 2016.  
1065 Melt-rock interaction near the Moho: Evidence from crystal cargo in lavas  
1066 from near-ridge seamounts. Geochimica et Cosmochimica Acta 191, 139–  
1067 164. doi:10.1016/j.gca.2016.07.017.
- 1068 Deer, W.A., Howie, R.A., Zussman, J., 1992. An introduction to the rock-  
1069 forming minerals. Longman Group Ltd, New York.

- 1070 Dostal, J., 2017. Rare earth element deposits of alkaline igneous rocks. *Re-*  
1071 *sources* 6, 1–12. doi:10.3390/resources6030034.
- 1072 Downes, H., Balaganskaya, E., Beard, A., Liferovich, R., Demaiffe, D.,  
1073 2005. Petrogenetic processes in the ultramafic, alkaline and carbonatitic  
1074 magmatism in the Kola Alkaline Province: A review. *Lithos* 85, 48–75.  
1075 doi:10.1016/j.lithos.2005.03.020.
- 1076 Droop, G.T.R., 1987. A general equation for estimating Fe<sup>3+</sup> concentrations  
1077 in ferromagnesian silicates and oxides from microprobe analyses, using  
1078 stoichiometric criteria. *Mineralogical magazine* 51, 431–435.
- 1079 Dygert, N., Liang, Y., Sun, C., Hess, P., 2014. An experimental study of  
1080 trace element partitioning between augite and Fe-rich basalts. *Geochimica  
1081 et Cosmochimica Acta* 132, 170–186. doi:10.1016/j.gca.2014.01.042.
- 1082 Edgar, C.J., Wolff, J.A., Olin, P.H., Nichols, H.J., Pittari, A., Cas, R.A.F.,  
1083 Reiners, P.W., Spell, T.L., Martí, J., 2007. The late Quaternary Diego Her-  
1084 nandez Formation, Tenerife: Volcanology of a complex cycle of voluminous  
1085 explosive phonolitic eruptions. *Journal of Volcanology and Geothermal Re-  
1086 search* 160, 59–85. doi:10.1016/j.jvolgeores.2006.06.001.
- 1087 Eugster, H.P., Wones, D.R., 1962. Stability relations of the ferruginous bi-  
1088 otite, annite. *Journal of Petrology* 3, 82–125. doi:10.1093/petrology/3.1.82.
- 1089 Fedele, L., Zanetti, A., Morra, V., Lustrino, M., Melluso, L., Vannucci,  
1090 R., 2009. Clinopyroxene/liquid trace element partitioning in natural  
1091 trachyte-trachyphonolite systems: insights from Campi Flegrei (south-

- ern Italy). Contributions to Mineralogy and Petrology 158, 337–356.  
doi:10.1007/s00410-009-0386-5.
- Foley, S.F., Prelevic, D., Rehfeldt, T., Jacob, D.E., 2013. Minor and trace elements in olivines as probes into early igneous and mantle melting processes. Earth and Planetary Science Letters 363, 181–191.  
doi:10.1016/j.epsl.2012.11.025.
- Francis, D., Minarik, W., 2008. Aluminum-dependent trace element partitioning in clinopyroxene. Contributions to Mineralogy and Petrology 156, 439–451. doi:10.1007/s00410-008-0295-z.
- Gaetani, G.A., 2004. The influence of melt structure on trace element partitioning near the peridotite solidus. Contributions to Mineralogy and Petrology 147, 511–527. doi:10.1007/s00410-004-0575-1.
- Gaetani, G.A., Grove, T.L., 1995. Partitioning of rare earth elements between clinopyroxene and silicate melt: Crystal-chemical controls. Geochimica et Cosmochimica Acta 59, 1951–1962. doi:10.1016/0016-7037(95)00119-0.
- Gaillard, F., Scaillet, B., Pichavant, M., 2002. Kinetics of iron oxidation-reduction in hydrous silicic melts. American Mineralogist 87, 829–837. doi:10.2138/am-2002-0704.
- Giehl, C., Marks, M., Nowak, M., 2013. Phase relations and liquid lines of descent of an iron-rich peralkaline phonolitic melt: an experimental study. Contributions to Mineralogy and Petrology 165, 283–304. doi:10.1007/s00410-012-0809-6.

- 1114 Giordano, D., Nichols, A., Dingwell, D., 2005. Glass transition temperatures  
1115 of natural hydrous melts: a relationship with shear viscosity and impli-  
1116 cations for the welding process. *Journal of Volcanology and Geothermal*  
1117 *Research* 142, 105–118. doi:10.1016/j.jvolgeores.2004.10.015.
- 1118 Girnis, A.V., Bulatov, V.K., Brey, G.P., Gerdes, A., Höfer, H.E., 2013. Trace  
1119 element partitioning between mantle minerals and silico-carbonate melts  
1120 at 6–12 GPa and applications to mantle metasomatism and kimberlite  
1121 genesis. *Lithos* 160-161, 183–200. doi:10.1016/j.lithos.2012.11.027.
- 1122 Goodenough, K.M., Schilling, J., Jonsson, E., Kalvig, P., Charles, N., Tuduri,  
1123 J., Deady, E.A., Sadeghi, M., Schiellerup, H., Müller, A., Bertrand, G.,  
1124 Arvanitidis, N., Eliopoulos, D.G., Shaw, R.A., Thrane, K., Keulen, N.,  
1125 2016. Europe's rare earth element resource potential: An overview of  
1126 REE metallogenetic provinces and their geodynamic setting. *Ore Geology  
1127 Reviews* 72, 838–856. doi:10.1016/j.oregeorev.2015.09.019.
- 1128 Grove, T.L., Baker, M.B., Kinzler, R.J., 1984. Coupled CaAl-NaSi dif-  
1129 fusion in plagioclase feldspar: Experiments and applications to cooling  
1130 rate speedometry. *Geochimica et Cosmochimica Acta* 48, 2113–2121.  
1131 doi:10.1016/0016-7037(84)90391-0.
- 1132 Guillou, H., Carracedo, J.C., Paris, R., Pérèz Torrado, F.J., 2004. Implica-  
1133 tions for the early shield-stage evolution of Tenerife from K/Ar ages and  
1134 magnetic stratigraphy. *Earth and Planetary Science Letters* 222, 599–614.  
1135 doi:10.1016/j.epsl.2004.03.012.
- 1136 Gurenko, A.A., Hoernle, K.A., Hauff, F., Schmincke, H.U., Han, D., Miura,

- 1137 Y.N., Kaneoka, I., 2006. Major, trace element and NdSrPbOHeAr isotope  
1138 signatures of shield stage lavas from the central and western Canary Is-  
1139 lands: Insights into mantle and crustal processes. *Chemical Geology* 233,  
1140 75–112. doi:10.1016/j.chemgeo.2006.02.016.
- 1141 Hanchar, J.M., Finch, R.J., Hoskin, P.W.O., Watson, E.B., Cher-  
1142 niak, D.J., Mariano, A.N., 2001. Rare earth elements in synthetic  
1143 zircon: Part 1. Synthesis, and rare earth element and phospho-  
1144 rus doping. *American Mineralogist* 86, 667–680. doi:10.1130/0091-  
1145 7613(1990)018;0757:CTOGAS;2.3.CO;2.
- 1146 Hazen, R.M., Finger, L.W., 1979. Bulk modulus-volume relationship for  
1147 cation-anion polyhedra. *Journal of Geophysical Research: Solid Earth* 84,  
1148 6723–6728. doi:10.1029/JB084iB12p06723.
- 1149 Hill, E., Blundy, J.D., Wood, B.J., 2011. Clinopyroxene-melt trace ele-  
1150 ment partitioning and the development of a predictive model for HFSE  
1151 and Sc. *Contributions to Mineralogy and Petrology* 161, 423–438.  
1152 doi:10.1007/s00410-010-0540-0.
- 1153 Hill, E., Wood, B.J., Blundy, J.D., 2000. The effect of Ca-Tschermaks com-  
1154 ponent on trace element partitioning between clinopyroxene and silicate  
1155 melt. *Lithos* 53, 203–215. doi:10.1016/S0024-4937(00)00025-6.
- 1156 Huang, F., Lundstrom, C.C., McDonough, W.F., 2006. Effect of melt  
1157 structure on trace-element partitioning between clinopyroxene and sili-  
1158 cic, alkaline, aluminous melts. *American Mineralogist* 91, 1385–1400.  
1159 doi:10.2138/am.2006.1909.

- 1160 Jugo, P.J., Wilke, M., Botcharnikov, R.E., 2010. Sulfur K-edge XANES anal-  
1161 ysis of natural and synthetic basaltic glasses: Implications for S speciation  
1162 and S content as function of oxygen fugacity. *Geochimica et Cosmochimica  
1163 Acta* 74, 5926–5938. doi:10.1016/j.gca.2010.07.022.
- 1164 Kennedy, A.K., Lofgren, G.E., Wasserburg, G.J., 1993. An experimental  
1165 study of trace element partitioning between olivine, orthopyroxene and  
1166 melt in chondrules: equilibrium values and kinetic effects. *Earth and Plan-  
1167 etary Science Letters* 115, 177–195. doi:10.1016/0012-821X(93)90221-T.
- 1168 Kogarko, L.N., 1990. Ore-forming potential of alkaline magmas. *Lithos* 26,  
1169 167–175. doi:10.1016/0024-4937(90)90046-4.
- 1170 Kovalenko, V.I., Hervig, R.L., Sheridan, M.F., 1988. Ion microprobe anal-  
1171 yses of trace elements in anorthoclase, hedenbergite, aenigmatite, quartz,  
1172 apatite and glass in pantellerite: evidence for high water contents in pan-  
1173 tellerite melt. *American Mineralogist* 73, 1038–1045.
- 1174 Kress, V.C., Carmichael, I.S.E., 1991. The compressibility of silicate liquids  
1175 containing Fe<sub>2</sub>O<sub>3</sub> and the effect of composition, temperature, oxygen fu-  
1176 gacity and pressure on their redox states. *Contributions to Mineralogy and  
1177 Petrology* 108, 82–92. doi:10.1007/BF00307328.
- 1178 Kumazawa, M., 1969. The elastic constants of single-crystal or-  
1179 thopyroxene. *Journal of Geophysical Research* 74, 5973–5980.  
1180 doi:10.1029/JB074i025p05973.
- 1181 Larsen, L.M., 1979. Distribution of REE and other trace elements between  
1182 phenocrysts and peralkaline undersaturated magmas, exemplified by rocks

- 1183 from the Gardar igneous province, south Greenland. *Lithos* 12, 303–315.  
1184 doi:10.1016/0024-4937(79)90022-7.
- 1185 Law, K.M., Blundy, J.D., Wood, B.J., Ragnarsdottir, K.V., 2000. Trace ele-  
1186 ment partitioning between wollastonite and silicate-carbonate melt. *Min-  
1187 eralogical Magazine* 64, 651–661. doi:10.1180/002646100549670.
- 1188 Liang, Y., Richter, F.M., Watson, E.B., 1994. Convection in multicom-  
1189 ponent silicate melts driven by coupled diffusion. *Nature* 369, 390–392.  
1190 doi:10.1038/369390a0.
- 1191 Linnen, R.L., Keppler, H., 1997. Columbite solubility in granitic melts:  
1192 consequences for the enrichment and fractionation of Nb and Ta in the  
1193 Earth's crust. *Contributions to Mineralogy and Petrology* 128, 213–227.  
1194 doi:10.1007/s004100050304.
- 1195 Lofgren, G., 1989. Dynamic crystallization of chondrule melts of porphyritic  
1196 olivine composition: Textures experimental and natural. *Geochimica et  
1197 Cosmochimica Acta* 53, 461–470. doi:10.1016/0016-7037(89)90397-9.
- 1198 Lofgren, G.E., Huss, G.R., Wasserburg, G.J., 2006. An experimental study  
1199 of trace-element partitioning between Ti-Al-clinopyroxene and melt: Equi-  
1200 librium and kinetic effects including sector zoning. *American Mineralogist*  
1201 91, 1596–1606. doi:10.2138/am.2006.2108.
- 1202 Lu, F., Anderson, A.T., Davis, A.M., 1995. Diffusional gradients at the crys-  
1203 tal / melt interface and their effect on the compositions of melt inclusions.  
1204 *The Journal of Geology* 103, 591–597.

- 1205 Lundstrom, C.C., Shaw, H.F., Ryerson, F.J., Phinney, D.L., Gill, J.B.,  
1206 Williams, Q., 1994. Compositional controls on the partitioning of U, Th,  
1207 Ba, Pb, Sr and Zr between clinopyroxene and haplobasaltic melts: impli-  
1208 cations for uranium series disequilibria in basalts. *Earth and Planetary*  
1209 *Science Letters* 128, 407–423. doi:10.1016/0012-821X(94)90159-7.
- 1210 Mahood, G.A., Stimac, J.A., 1990. Trace-element partitioning in pantel-  
1211 lerites and trachytes. *Geochimica et Cosmochimica Acta* 54, 2257–2276.  
1212 doi:10.1016/0016-7037(90)90050-U.
- 1213 Marks, M., Halama, R., Wenzel, T., Markl, G., 2004. Trace element vari-  
1214 ations in clinopyroxene and amphibole from alkaline to peralkaline syen-  
1215 ites and granites: implications for mineral-melt trace-element partitioning.  
1216 *Chemical Geology* 211, 185–215. doi:10.1016/j.chemgeo.2004.06.032.
- 1217 Marks, M., Markl, G., 2001. Fractionation and assimilation processes in the  
1218 alkaline augite syenite unit of the Ilímaussaq intrusion, south Greenland,  
1219 as deduced from phase equilibria. *Journal of Petrology* 42, 1947–1969.  
1220 doi:10.1093/petrology/42.10.1947.
- 1221 Marks, M., Markl, G., 2003. Ilímaussaq en miniature': closed-system frac-  
1222 tionation in an agpaitic dyke rock from the Gardar Province, South Green-  
1223 land (contribution to the mineralogy of Ilímaussaq no. 117). *Mineralogical*  
1224 *Magazine* 67, 893–919. doi:10.1180/0026461036750150.
- 1225 Marks, M.A., Markl, G., 2017. A global review on agpaitic rocks. *Earth-*  
1226 *Science Reviews* 173, 229–258. doi:10.1016/j.earscirev.2017.06.002.

- 1227 Marks, M.A.W., Hettmann, K., Schilling, J., Frost, B.R., Markl, G., 2011.  
1228 The mineralogical diversity of alkaline igneous rocks: Critical factors for  
1229 the transition from miaskitic to agpaitic phase assemblages. *Journal of*  
1230 *Petrology* 52, 439–455. doi:10.1093/petrology/egq086.
- 1231 Möller, V., Williams-Jones, A.E., 2016. Petrogenesis of the Necha-  
1232 lacho Layered Suite, Canada: magmatic evolution of a REE-Nb-  
1233 rich nepheline syenite intrusion. *Journal of Petrology* 57, 229–276.  
1234 doi:10.1093/petrology/egw003.
- 1235 Mollo, S., Blundy, J.D., Giacomoni, P., Nazzari, M., Scarlato, P., Coltorti,  
1236 M., Langone, A., Andronico, D., 2017. Clinopyroxene-melt element par-  
1237 titioning during interaction between trachybasaltic magma and siliceous  
1238 crust: Clues from quartzite enclaves at Mt. Etna volcano. *Lithos* 284-285,  
1239 447–461. doi:10.1016/j.lithos.2017.05.003.
- 1240 Mollo, S., Blundy, J.D., Iezzi, G., Scarlato, P., Langone, A., 2013. The  
1241 partitioning of trace elements between clinopyroxene and trachybasaltic  
1242 melt during rapid cooling and crystal growth. *Contributions to Mineralogy*  
1243 and *Petrology* 166, 1633–1654. doi:10.1007/s00410-013-0946-6.
- 1244 Mollo, S., Forni, F., Bachmann, O., Blundy, J.D., De Astis, G., Scarlato,  
1245 P., 2016. Trace element partitioning between clinopyroxene and trachy-  
1246 phonolitic melts: A case study from the Campanian Ignimbrite (Campi  
1247 Flegrei, Italy). *Lithos* 252253, 160–172. doi:10.1016/j.lithos.2016.02.024.
- 1248 Moore, G., Vennemann, T., Carmichael, I.S.E., 1998. An empirical model

- 1249 for the solubility of H<sub>2</sub>O in magmas to 3 kilobars. American Mineralogist  
1250 83, 36–42. doi:10.1016/0012-821X(73)90129-5.
- 1251 Morimoto, N., 1989. Nomenclature of pyroxenes. Mineralogical Journal 14,  
1252 198–221. doi:10.2465/minerj.14.198.
- 1253 Mungall, J., Brenan, J., 2014. Partitioning of platinum-group elements and  
1254 Au between sulfide liquid and basalt and the origins of mantle-crust frac-  
1255 tionation of the chalcophile elements. Geochimica et Cosmochimica Acta  
1256 125, 265–289. doi:10.1016/j.gca.2013.10.002.
- 1257 Mysen, B.O., Virgo, D., Seifert, F.A., 1982. The structure of silicate melts:  
1258 Implications for chemical and physical properties of natural magma. Re-  
1259 views of Geophysics 20, 353–383. doi:10.1029/RG020i003p00353.
- 1260 Mysen, B.O., Virgo, D., Seifert, F.A., 1985. Relationships between properties  
1261 and structure of aluminosilicate melts. American Mineralogist 70, 88–105.  
1262 doi:10.1007/BF00413348.
- 1263 Niu, Y., 2004. Bulk-rock major and trace element compositions of abyssal  
1264 peridotites: Implications for mantle melting, melt extraction and post-  
1265 melting processes beneath Mid-Ocean ridges. Journal of Petrology 45,  
1266 2423–2458. doi:10.1093/petrology/egh068.
- 1267 Olin, P.H., Wolff, J.A., 2010. Rare earth and high field strength element par-  
1268 titioning between iron-rich clinopyroxenes and felsic liquids. Contributions  
1269 to Mineralogy and Petrology 160, 761–775. doi:10.1007/s00410-010-0506-2.
- 1270 Onuma, N., Higuchi, H., Wakita, H., Nagasawa, H., 1968. Trace element

- partition between two pyroxenes and the host lava. *Earth and Planetary Science Letters* 5, 47–51. doi:10.1016/S0012-821X(68)80010-X.
- Paton, C., Hellstrom, J., Paul, B., Woodhead, J., Hergt, J., 2011. Iolite: Freeware for the visualisation and processing of mass spectrometric data. *Journal of Analytical Atomic Spectrometry* 26, 2508–2518. doi:10.1039/C1JA10172B.
- Peters, S.T., Troll, V.R., Weis, F.A., Dallai, L., Chadwick, J.P., Schulz, B., 2017. Amphibole megacrysts as a probe into the deep plumbing system of Merapi volcano, Central Java, Indonesia. *Contributions to Mineralogy and Petrology* 172, 1–20. doi:10.1007/s00410-017-1338-0.
- Prowatke, S., Klemme, S., 2005. Effect of melt composition on the partitioning of trace elements between titanite and silicate melt. *Geochimica et Cosmochimica Acta* 69, 695–709. doi:10.1016/j.gca.2004.06.037.
- Putirka, K.D., 2008. Thermometers and Barometers for Volcanic Systems. *Reviews in Mineralogy and Geochemistry* 69, 61–120. doi:10.2138/rmg.2008.69.3.
- Rapp, R.P., Watson, E.B., 1986. Monazite solubility and dissolution kinetics: implications for the thorium and light rare earth chemistry of felsic magmas. *Contributions to Mineralogy and Petrology* 94, 304–316. doi:10.1007/BF00371439.
- Rasband, W., 2016. ImageJ, U.S. National Institutes of Health, Bethesda, Maryland, USA.

- 1293 Redhammer, G.J., Amthauer, G., Roth, G., Tippelt, G., Lotter-  
1294 moser, W., 2006. Single-crystal X-ray diffraction and temperature  
1295 dependent  $^{57}\text{Fe}$  Mössbauer spectroscopy on the hedenbergite-aegirine  
1296  $(\text{Ca},\text{Na})(\text{Fe}^{2+},\text{Fe}^{3+})\text{Si}_2\text{O}_6$  solid solution. American Mineralogist 91,  
1297 1271–1292. doi:10.2138/am.2006.2173.
- 1298 Reguir, E.P., Chakhmouradian, A.R., Pisiak, L., Halden, N.M., Yang, P.,  
1299 Xu, C., Kynický, J., Couëslan, C.G., 2012. Trace-element composition  
1300 and zoning in clinopyroxene- and amphibole-group minerals: Implications  
1301 for element partitioning and evolution of carbonatites. Lithos 128, 27–45.  
1302 doi:10.1016/j.lithos.2011.10.003.
- 1303 Rubatto, D., Hermann, J., 2007. Experimental zircon/melt and  
1304 zircon/garnet trace element partitioning and implications for the  
1305 geochronology of crustal rocks. Chemical Geology 241, 38–61.  
1306 doi:10.1016/j.chemgeo.2007.01.027.
- 1307 Schmidt, B.C., Behrens, H., 2008. Water solubility in phonolite melts: Influ-  
1308 ence of melt composition and temperature. Chemical Geology 256, 259–  
1309 268. doi:10.1016/j.chemgeo.2008.06.043.
- 1310 Schmidt, K.H., Bottazzi, P., Vannucci, R., Mengel, K., 1999. Trace element  
1311 partitioning between phlogopite, clinopyroxene and leucite lamproite melt.  
1312 Earth and Planetary Science Letters 168, 287–299. doi:10.1016/S0012-  
1313 821X(99)00056-4.
- 1314 Schmidt, M.W., Connolly, J.A.D., Günther, D., Bogaerts, M., 2006. Element

- partitioning: The role of melt structure and composition. *Science* 312, 1646–1650. doi:10.1126/science.1126690.
- Severs, M.J., Beard, J.S., Fedele, L., Hanchar, J.M., Mutchler, S.R., Bodnar, R.J., 2009. Partitioning behavior of trace elements between dacitic melt and plagioclase, orthopyroxene, and clinopyroxene based on laser ablation ICPMS analysis of silicate melt inclusions. *Geochimica et Cosmochimica Acta* 73, 2123–2141. doi:10.1016/j.gca.2009.01.009.
- Shannon, R., 1976. Revised effective ionic radii and systematic studies of interatomic distances in halides and chalcogenides. *Acta Crystallographica Section A* 32, 751–767.
- Shea, T., Hammer, J.E., 2013. Kinetics of cooling- and decompression-induced crystallization in hydrous mafic-intermediate magmas. *Journal of Volcanology and Geothermal Research* 260, 127–145. doi:10.1016/j.jvolgeores.2013.04.018.
- Shearer, C.K., Larsen, L.M., 1994. Sector-zoned aegirine from the Ilimaussaq alkaline intrusion, South Greenland; implications for trace-element behavior in pyroxene. *American Mineralogist* 79, 340–352.
- Sjöqvist, A., Cornell, D., Andersen, T., Erambert, M., Ek, M., Leijd, M., 2013. Three compositional varieties of rare-earth element ore: Eudialyte-group minerals from the Norra Kärr alkaline complex, Southern Sweden. *Minerals* 3, 94–120. doi:10.3390/min3010094.
- Sørensen, H., 1992. Agpaitic nepheline syenites: a potential source of

- 1337 rare elements. *Applied Geochemistry* 7, 417–427. doi:10.1016/0883-  
1338 2927(92)90003-L.
- 1339 Spera, F.J., Bohrson, W.A., 2001. Energy-constrained open-system mag-  
1340 matic processes I: General model and energy-constrained assimilation and  
1341 fractional crystallization (EC-AFC) formulation. *Journal of Petrology* 42,  
1342 999–1018. doi:10.1093/petrology/42.5.999.
- 1343 Stevens, J., 1996. Applied multivariate analysis for the social sciences.  
1344 Lawrence Erlbaum, Mahwah, NJ.
- 1345 Sun, C., Liang, Y., 2012. Distribution of REE between clinopyroxene and  
1346 basaltic melt along a mantle adiabat: Effects of major element composi-  
1347 tion, water, and temperature. *Contributions to Mineralogy and Petrology*  
1348 163, 807–823. doi:10.1007/s00410-011-0700-x.
- 1349 Thirlwall, M.F., Singer, B.S., Marriner, G.F., 2000.  $^{39}\text{Ar}$ - $^{40}\text{Ar}$  ages and  
1350 geochemistry of the basaltic shield stage of Tenerife, Canary Islands,  
1351 Spain. *Journal of Volcanology and Geothermal Research* 103, 247–297.  
1352 doi:10.1016/S0377-0273(00)00227-4.
- 1353 Troll, V., Schmincke, H., 2002. Magma mixing and crustal recycling recorded  
1354 in ternary feldspar from compositionally zoned peralkaline ignimbrite  
1355 'A', Gran Canaria, Canary Islands. *Journal of Petrology* 43, 243–270.  
1356 doi:10.1093/petrology/43.2.243.
- 1357 Van Orman, J.A., Grove, T.L., Shimizu, N., 2001. Rare earth element diffu-  
1358 sion in diopside: influence of temperature, pressure, and ionic radius, and

- 1359        an elastic model for diffusion in silicates. Contributions to Mineralogy and  
1360        Petrology 141, 687–703. doi:10.1007/s004100100269.
- 1361        Walker, D., Kirkpatrick, R.J., Longhi, J., Hays, J.F., 1976. Crystallization  
1362        history of lunar picritic basalt sample 12002: Phase-equilibria and cooling-  
1363        rate studies. Bulletin of the Geological Society of America 87, 646–656.  
1364        doi:10.1130/0016-7606(1976)87;646:CHOLPB;2.0.CO;2.
- 1365        Watson, E.B., 1979. Zircon saturation in felsic liquids: Experimental results  
1366        and applications to trace element geochemistry. Contributions to Miner-  
1367        alogy and Petrology 70, 407–419. doi:10.1007/BF00371047.
- 1368        Weidner, D.J., Vaughan, M.T., 1982. Elasticity of pyroxenes: Effects of  
1369        composition versus crystal structure. Journal of Geophysical Research 87,  
1370        9349–9353.
- 1371        Wiesmaier, S., Troll, V.R., Carracedo, J.C., Ellam, R.M., Bindeman, I.,  
1372        Wolff, J.A., 2012. Bimodality of lavas in the Teide–Pico Viejo Succession  
1373        in Tenerife—the role of crustal melting in the origin of recent phonolites.  
1374        Journal of Petrology 53, 2465–2495. doi:10.1093/petrology/egs056.
- 1375        Wood, B.J., Blundy, J.D., 1997. A predictive model for rare earth  
1376        element partitioning between clinopyroxene and anhydrous silicate  
1377        melt. Contributions to Mineralogy and Petrology 129, 166–181.  
1378        doi:10.1007/s004100050330.
- 1379        Wood, B.J., Blundy, J.D., 2001. The effect of cation charge on crystal–melt  
1380        partitioning of trace elements. Earth and Planetary Science Letters 188,  
1381        59–71. doi:10.1016/S0012-821X(01)00294-1.

- 1382 Wood, B.J., Blundy, J.D., 2003. Trace element partitioning under crustal  
1383 and uppermost mantle conditions: The influences of ionic radius, cation  
1384 charge, pressure, and temperature, in: Carlson, R.W. (Ed.), *The Mantle*  
1385 and Core: Treatise on Geochemistry. Elsevier. volume 2. chapter 2.09, pp.  
1386 395–424. doi:10.1016/B0-08-043751-6/02009-0.
- 1387 Wood, B.J., Blundy, J.D., 2014. Trace element partitioning: The influences  
1388 of ionic radius, cation charge, pressure, and temperature, in: Carlson,  
1389 R.W. (Ed.), *The Mantle and Core: Treatise on Geochemistry: Second Edition*.  
1390 Elsevier. chapter 3.11, pp. 421–445. doi:10.1016/B978-0-08-095975-  
1391 7.00206-0.
- 1392 Wood, B.J., Trigila, R., 2001. Experimental determination of aluminous  
1393 clinopyroxene–melt partition coefficients for potassic liquids, with applica-  
1394 tion to the evolution of the Roman province potassic magmas. *Chemical*  
1395 *Geology* 172, 213–223. doi:10.1016/S0009-2541(00)00259-X.
- 1396 Workman, R.K., Hart, S.R., 2005. Major and trace element composition of  
1397 the depleted MORB mantle (DMM). *Earth and Planetary Science Letters*  
1398 231, 53–72. doi:10.1016/j.epsl.2004.12.005.
- 1399 Wörner, G., Beusen, J.M., Duchateau, N., Gijbels, R., Schmincke, H.U.,  
1400 1983. Trace element abundances and mineral/melt distribution coefficients  
1401 in phonolites from the Laacher See volcano (Germany). *Contributions to*  
1402 *Mineralogy and Petrology* 84, 152–173. doi:10.1007/BF00371282.
- 1403 Xu, C., Kynicky, J., Chakhmouradian, A.R., Campbell, I.H., Allen, C.M.,  
1404 2010. Trace-element modeling of the magmatic evolution of rare-earth-rich

- 1405 carbonatite from the Miaoya deposit, Central China. *Lithos* 118, 145–155.
- 1406 doi:10.1016/j.lithos.2010.04.003.
- 1407 Yao, L., Sun, C., Liang, Y., 2012. A parameterized model for REE distri-  
1408 bution between low-Ca pyroxene and basaltic melts with applications to  
1409 REE partitioning in low-Ca pyroxene along a mantle adiabat and dur-  
1410 ing pyroxenite-derived melt and peridotite interaction. *Contributions to  
1411 Mineralogy and Petrology* 164, 261–280. doi:10.1007/s00410-012-0737-5.
- 1412 Zhang, Y., Ni, H., Chen, Y., 2010. Diffusion data in silicate melts. *Reviews  
1413 in Mineralogy and Geochemistry* 72, 311–408. doi:10.2138/rmg.2010.72.8.

<sup>1414</sup> **6. Tables**

Table 1: Major-element composition (in wt%) of starting materials for the internally heated pressure vessel experiments. The totals are calculated with all iron as FeO.

*Dry starting glass compositions calculated from masses of reagents added [wt%]*

Composition	SiO <sub>2</sub>	TiO <sub>2</sub>	Al <sub>2</sub> O <sub>3</sub>	FeOT	MgO	CaO	Na <sub>2</sub> O	K <sub>2</sub> O	Total	(Na+K)/Al
L4	57.48	1.50	19.00	5.89	1.61	3.21	7.33	3.98	100.00	0.861
L5	61.24	0.68	19.51	3.77	0.43	0.91	8.63	4.84	100.00	0.996
M3	52.67	2.27	18.13	7.86	2.75	5.40	7.19	3.73	100.00	0.875
M4	56.35	1.47	18.63	5.77	1.58	3.15	8.48	4.57	100.00	1.014
M5	60.04	0.66	19.13	3.69	0.42	0.89	9.76	5.41	100.00	1.145
H4	54.80	1.43	18.12	5.62	1.54	3.06	10.07	5.38	100.00	1.236
H5	58.38	0.65	18.60	3.59	0.41	0.86	11.31	6.20	100.00	1.362

*Water saturated glass compositions from superliquidus experiments (EPMA) [wt%]*

L5	57.46	0.643	16.59	2.363	0.404	0.985	7.840	4.462	90.75	1.069
s.d. (n = 8)	0.299	0.087	0.210	0.059	0.035	0.050	0.175	0.132	0.351	0.017
rsd	0.52%	13.58%	1.26%	2.51%	8.70%	5.09%	2.23%	2.97%	0.39%	1.57%
H5	55.58	0.612	16.21	2.568	0.422	0.906	10.77	5.732	92.80	1.476
s.d. (n = 13)	0.327	0.057	0.221	0.113	0.044	0.049	0.205	0.154	0.417	0.028
rsd	0.59%	9.33%	1.36%	4.41%	10.44%	5.40%	1.90%	2.69%	0.45%	1.87%

Table 2: Summary of run conditions and run products for the internally-heated pressure vessel experiments.

Experiment	Setup	Pressure [bar]	Cooling ramp				(after ramp) [h,m]	Run products
			Rate °C /min	Cycle +10°C	TE-1/TE-3 [°C ]	TE-2 (spl) [°C ]		
L4 <sub>3</sub>	IHPV RQ (f)	2038	1	Y	825	828	44h50m	Cpx + Ox + Ttn + Melt
L5 <sub>3</sub>	IHPV RQ (f)	2038	1	Y	825	828	44h50m	Cpx + Ox + Melt
M3 <sub>2</sub>	IHPV RQ	2020	1	Y	796/795	799	47h	Cpx + Ox + Bt + Melt
M4 <sub>4</sub>	IHPV RQ	2020	1	Y	796/795	799	47h	Cpx + Ox + Bt + Melt
M5	IHPV	2000	-	-	800	799	47h55m	Cpx + Bt + Fsp + Melt
M5 <sub>2</sub>	IHPV RQ	2000	-	-	700	689	45h45m	Cpx + Bt + Fsp + Melt
H4 <sub>2</sub>	IHPV	2000	-	-	800	799	47h55m	Cpx + Ttn + Melt
H5 <sub>2</sub>	IHPV RQ	2000	-	-	700	689	45h45m	Cpx + Bt + Fsp + Melt
H5 <sub>3</sub>	IHPV RQ	2020	-	-	651/649	648	46h15m	Cpx + Bt + Fsp + Melt
NLS-9	IHPV RQ	2020	1	Y	651/649	648	46h15m	Cpx + Ox + Melt
NLS-9 <sub>2</sub> HM	IHPV RQ**	2000	1	Y	650	655	42h	Cpx + Ox + Fsp + Melt

(f) indicates failure of the rapid quench apparatus; \*\* indicates use of a haematite double capsule, for run conditions at the haematite-magnetite  $f\text{O}_2$  buffer (Eugster and Wones, 1962). Cpx = clinopyroxene; Ox = spinel oxide; Ttn = titanite; Bt = biotite; Fsp = sanidine feldspar.

Table 3: Representative major-element compositions of clinopyroxene and melt for the performed internally heated pressure vessel experiments and Canary Islands phenocryst–glass pairs.

<i>Pyroxene</i>	L4 <sub>3</sub>	M3 <sub>2</sub>	M5 <sub>2</sub>	H5 <sub>3</sub>	NLS-9	NLS-9 <sub>2</sub> HM	16-07 LMB	17-12 M. Samara	17-14 UMB-II	21-30 PV 2 ka
SiO <sub>2</sub>	44.70	40.73	47.31	46.95	50.73	51.90	52.43	51.77	51.81	52.50
TiO <sub>2</sub>	3.07	4.57	3.17	4.47	0.10	0.10	0.80	0.78	0.74	0.75
Al <sub>2</sub> O <sub>3</sub>	5.23	9.26	3.08	3.10	2.46	2.96	1.33	1.24	1.27	1.22
FeO	13.31	11.72	18.84	16.95	28.14	28.61	9.71	9.62	10.51	10.02
MnO	0.01	0.01	0.01	0.00	0.25	0.17	0.78	0.84	0.91	0.81
MgO	9.09	9.28	5.55	6.05	0.05	0.07	12.30	12.64	12.07	11.88
CaO	19.49	22.17	16.11	15.29	5.88	3.14	21.90	21.76	21.52	22.02
Na <sub>2</sub> O	2.27	1.01	4.34	4.97	9.86	11.45	1.18	1.17	1.38	1.19
K <sub>2</sub> O	0.09	0.03	0.08	0.07	0.04	0.04	0.02	0.03	0.00	0.02
Total	97.25	98.78	98.49	97.85	97.49	98.45	100.44	99.85	100.22	100.42
<i>Glass</i>										
SiO <sub>2</sub>	58.79	57.29	57.45	54.91	58.17	58.14	60.38	55.10	59.08	60.04
TiO <sub>2</sub>	0.35	0.27	0.23	0.62	0.00	0.00	0.64	1.73	0.66	0.66
Al <sub>2</sub> O <sub>3</sub>	17.35	19.14	16.69	16.06	18.55	19.41	19.96	18.30	19.68	19.79
Fe <sub>2</sub> O <sub>3</sub> (T)	2.35	1.35	1.01	3.16	1.67	1.91	3.65	7.22	4.02	3.96
FeO(T)	2.12	1.22	0.91	2.84	1.50	1.72	3.28	6.49	3.62	3.56
MnO	0.02	0.00	-	0.01	0.06	0.04	0.14	0.23	0.22	0.20
MgO	0.20	0.13	0.15	0.35	0.00	0.00	0.39	1.84	0.32	0.35
CaO	0.55	0.95	0.24	0.84	0.23	0.23	0.76	4.10	0.77	0.74
Na <sub>2</sub> O	7.17	7.32	9.08	8.88	11.12	9.80	9.00	7.26	9.76	9.05
K <sub>2</sub> O	4.68	4.10	4.68	5.30	1.51	2.51	5.41	4.09	5.45	5.57
Total	91.23	90.41	89.43	89.81	91.15	91.85	99.95	99.13	99.56	99.95
(Na+K)/Al	0.97	0.86	1.15	1.27	1.07	0.97	1.01	1.12	1.09	1.09

Table 4: Pyroxene-melt trace-element-partition coefficients for representative experiments and a natural phenocryst-glass pair.

-	L4 <sub>3</sub>		M3 <sub>2</sub>		M5 <sub>2</sub>		H5 <sub>3</sub>		NLS-9		NLS-9 <sub>2</sub> HM		16-07-px4 LMB	
	D	$\sigma$	D	$\sigma$	D	$\sigma$	D	$\sigma$	D	$\sigma$	D	$\sigma$	D	$\sigma$
Li	0.250	0.016	0.126	0.009	0.419	0.034	0.427	0.024	0.274	0.029	0.251	0.025	0.157	0.021
Ga	0.364	0.022	0.567	0.020	0.190	0.022	-	-	-	-	-	-	0.216	0.020
Rb	0.005	0.002	0.018	0.003	0.010	0.006	0.013	0.002	0.026	0.015	-	-	0.000	0.000
Sr	0.828	0.045	0.282	0.024	1.433	0.111	0.997	0.091	0.321	0.045	0.269	0.111	0.732	0.293
Y	5.577	0.302	13.784	1.949	1.814	0.236	1.102	0.060	0.482	0.048	0.713	0.070	2.183	0.232
Zr	1.699	0.082	2.537	0.222	1.361	0.089	1.164	0.083	2.102	0.196	3.895	0.482	0.434	0.047
Nb	0.126	0.085	0.889	0.258	0.554	0.280	1.688	0.196	2.382	0.294	9.642	4.015	0.0062	0.0004
Cs	0.019	0.003	0.019	0.003	0.014	0.006	0.010	0.002	-	-	0.023	0.017	0.001	0.001
Ba	0.0364	0.0087	0.0373	0.0152	0.0388	0.0261	0.0288	0.0091	-	-	-	-	0.00004	0.00004
La	4.787	0.646	2.591	0.240	4.658	0.962	3.049	0.132	0.410	0.037	0.542	0.043	0.769	0.071
Ce	7.199	0.756	6.229	0.646	5.199	1.073	3.190	0.129	0.377	0.028	0.547	0.061	1.591	0.120
Nd	16.105	1.537	28.430	4.210	6.454	1.630	3.759	0.147	0.579	0.054	0.925	0.114	2.632	0.155
Sm	17.843	1.414	47.245	7.699	5.215	1.293	3.113	0.137	0.388	0.070	0.767	0.182	3.522	0.421
Eu	16.403	1.341	53.195	8.181	4.743	1.132	2.900	0.133	0.275	0.082	0.682	0.192	3.372	0.196
Dy	9.027	0.537	27.082	3.925	2.619	0.460	1.521	0.073	0.329	0.057	0.388	0.088	2.798	0.220
Tm	4.773	0.261	9.067	0.903	2.937	0.279	1.567	0.097	1.330	0.145	2.860	0.890	1.846	0.182
Yb	4.797	0.249	7.015	0.600	3.937	0.296	2.281	0.152	2.564	0.346	8.004	3.116	1.978	0.186
Hf	2.385	0.162	3.556	0.472	1.802	0.118	1.141	0.123	2.443	0.275	3.702	0.479	0.769	0.065
Ta	0.496	0.152	2.3694	0.6244	0.6502	0.2545	1.5654	0.2337	2.1082	0.1764	3.6854	0.6561	0.0153	0.0013
Pb	0.079	0.017	0.0587	0.0152	0.1142	0.0349	0.0199	0.0130	0.0884	0.0280	0.0564	0.0536	0.0203	0.0040
Th	0.201	0.034	0.3565	0.0419	0.3172	0.0321	0.2892	0.0239	0.0798	0.0240	0.0709	0.0276	0.0040	0.0003
U	-	-	0.0512	0.0331	0.1261	0.0272	0.0196	0.0103	0.0460	0.0245	0.0834	0.0342	0.0022	0.0003

Table 5: Coefficients for prediction of lattice-strain parameters for clinopyroxene M1 and M2 sites from clinopyroxene composition, temperature and pressure. Fitted vs. predicted lattice-strain parameters and partition coefficients are in Figures 12–13 and full multiple linear regression reports are available as supplementary data file S4.

Model for $\text{Ln}D_0$ M2 site (n = 82)			Model for $\text{Ln}D_0$ , M1 site (n = 16)		
Parameter	Coefficient	$\sigma$	Parameter	Coefficient	$\sigma$
Intercept	4.52	0.91	Intercept	5	1
M1Ti	6.8	3	TAl	4	0.5
M1Al - M1Fe <sup>3+</sup>	1.6	0.6	M1Fe <sup>2+</sup>	2.6	0.9
M2Fe <sup>2+</sup>	-3.8	1.3	M2Na	-8	1
T [K]	-0.0035	0.0007	M2Ca	-3	2
TAl + TFe <sup>3+</sup>	2.6	0.8			
$R^2$		0.647			0.959

Model for $E_s$ , M2 site (n = 79)			Model for $E_s$ , M1 site (n = 18)		
Parameter	Coefficient	$\sigma$	Parameter	Coefficient	$\sigma$
Intercept	247	44	Intercept	-2322	298
M1Al	-424	144	T [K]	3.2	0.4
M1Mg	-285	102	P [GPa]	-408	145
M1Ti	-1145	378	M1Mg	-800	212
M2Mg	-306	115			
P [GPa]	37	12			
TAl + TFe <sup>3+</sup>	313	102			
XMg	336	102			
$R^2$		0.348			0.936

Model for $r_0$ , M2 site (n = 82)			Model for $r_0$ , M1 site (n = 16)		
Parameter	Coefficient	$\sigma$	Parameter	Coefficient	$\sigma$
Intercept	1.01	0.02	Intercept	0.79	0.03
M1Ti	0.16	0.05	P [GPa]	-0.017	0.005
M1Al-M1Fe <sup>3+</sup>	-0.03	0.01	M2Mg	-0.48	0.06
M2Ca	0.09	0.02	M1Fe <sup>3+</sup>	0.14	0.03
M2Na	0.14	0.02	M2Ca	-0.05	0.02
T [K]	-4.46E-05	1.22E-05			
$R^2$		0.846			0.987

1415 7. Supplementary figures

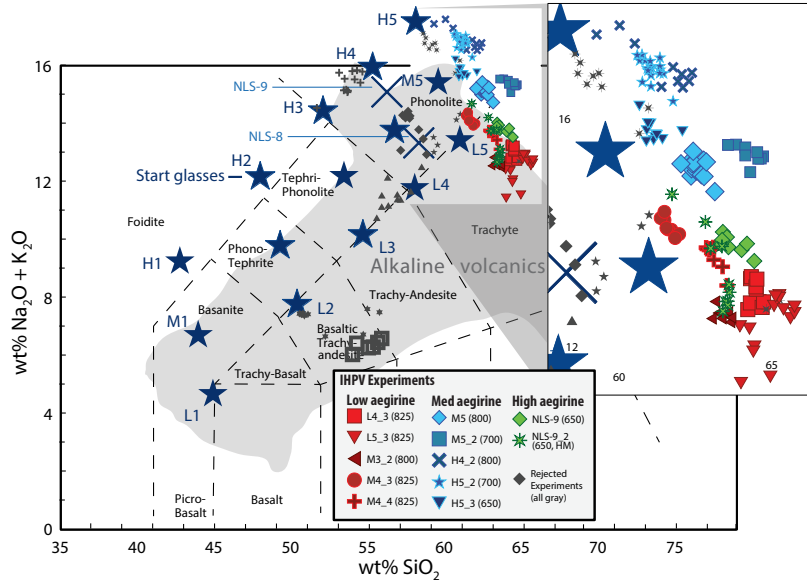


Figure S1: Total alkalies silica diagram for glasses produced in internally heated pressure vessel experiments. Large stars indicate synthetic starting glass compositions as used in internally heated pressure vessel experiments (Table 1). The gray field indicates the compositional range expressed by alkaline volcanic provinces from around the world, sourced from the GEOREM database. Full references in Supplement S1. Rejected experiments in dark gray are not discussed in the main text, and either did not produce clinopyroxene, produced crystals that were too small for analysis by LA-ICP-MS, or grew crystals during quench, hence preserving disequilibrium partitioning behaviour.

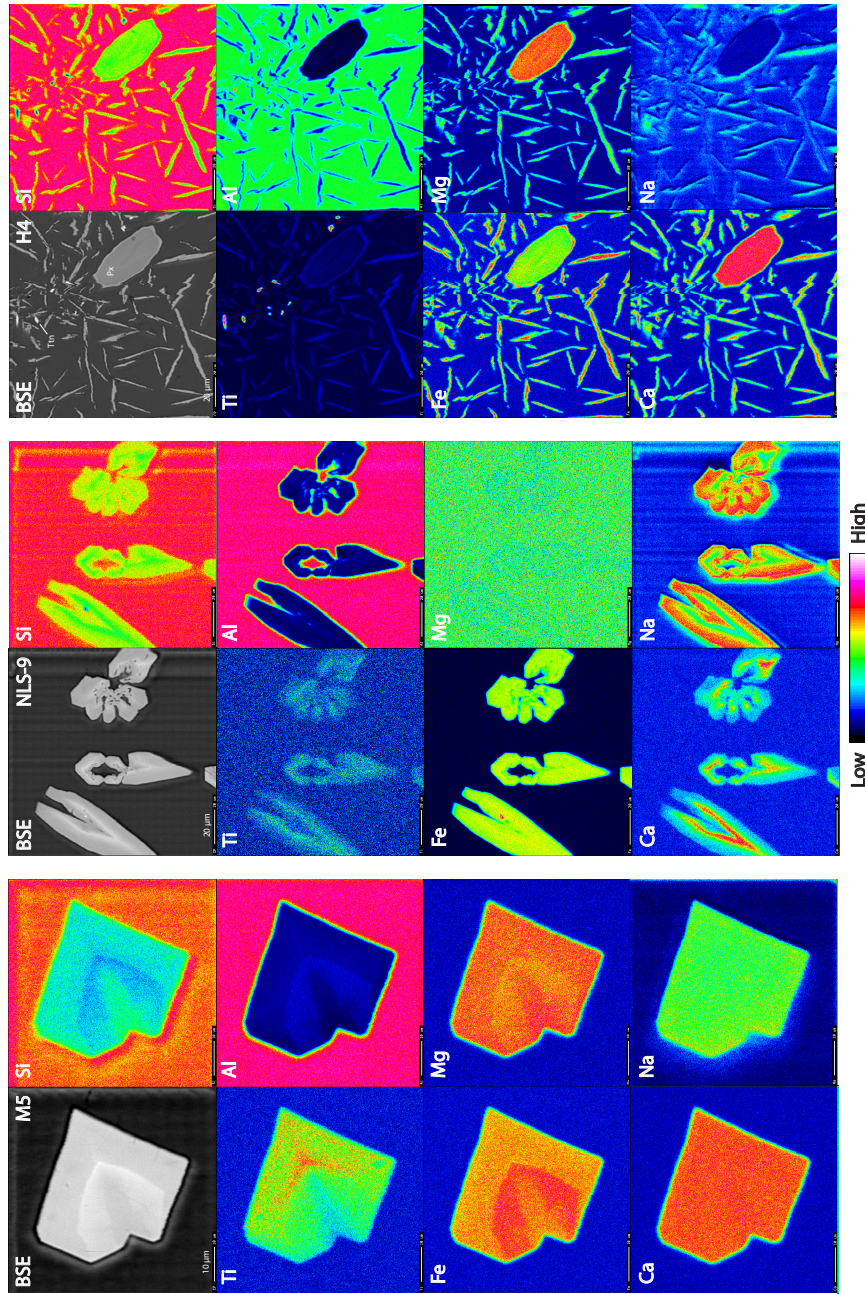


Figure S2: Element maps of clinopyroxene from internally heated pressure vessel experiments. M5 clinopyroxene have a sharp internal boundary that reflects feldspar saturation and are subtly zoned. NLS-9 clinopyroxene are more strongly zoned with swallowtail and hopper textures and rare inclusions of magnetite (cf. Walker et al., 1976; Lofgren, 1989; Shea and Hammer, 2013). H4 clinopyroxene ( $P_X$ ) display a bimodal crystal size distribution and occur with titanite (Tn). The bimodal crystal size distribution is due to a temperature perturbation during run, and renders this experiment unsuitable for this element partitioning study.

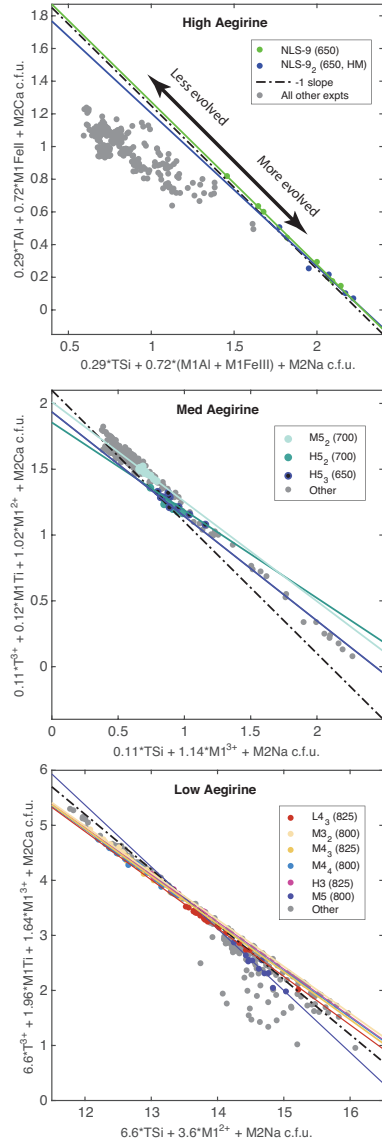


Figure S3: Major-element exchange mechanisms for (a) high, (b) medium and (c) low-aegirine clinopyroxene generated in internally heated pressure vessel experiments. Each individual plotted point represents an electron-microprobe analysis. Axes were defined by linear regressions between site assigned element abundances, which have been checked for consistency in total site occupancy and charge.

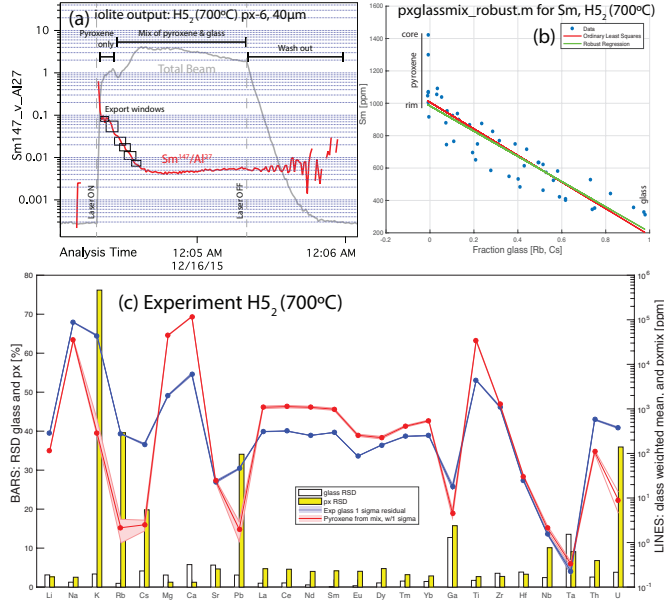


Figure S4: An example of the robust regression data reduction scheme for laser-ablation ICP-MS analyses of glass and clinopyroxene mixtures. (a) Time series of laser-ablation data, showing traces for Sm/Al (red) and total beam intensity (gray). The laser beam often ablated through the small clinopyroxene crystals, returning a mixed signal, that was exported from the iolite data reduction software in short time windows, as shown. Data were then normalised to the sum of major-element concentrations and mixes were deconvolved using a robust regression script written in MATLAB. (b) An example output diagram for the robust regression data reduction scheme. clinopyroxene-glass mixing ratios were constrained by strongly incompatible elements Rb and Cs. For each element, a robust linear regression was defined between the fraction of glass in the mixture, and element concentration. The intercept of this regression with zero glass returned the trace-element concentrations in the clinopyroxene. Uncertainty with this technique is typically below 10 % relative (median 9.3 % at the  $1\sigma$  level). In this example, the Sm-rich core of a zoned clinopyroxene crystal is effectively rejected during data processing, and the derived Sm concentration for the clinopyroxene is lower, therefore closer to that of the rims.(c) A quality control diagram output from the MATLAB data reduction scheme, showing the concentrations of various elements in the glass and clinopyroxene (lines) and the uncertainty on these concentrations expressed as a relative standard deviation (bars). Derived partition coefficients ( $D_i$ ) are the mass concentration of element ' $i$ ' in clinopyroxene divided by that in the adjacent quenched melt. Residuals for the  $D_i$  values were calculated using uncertainties derived from the clinopyroxene and glass analyses to calculate minimum and maximum partition coefficients at the  $1\sigma$  level. These are reported in Table 4 and Supplement S1.

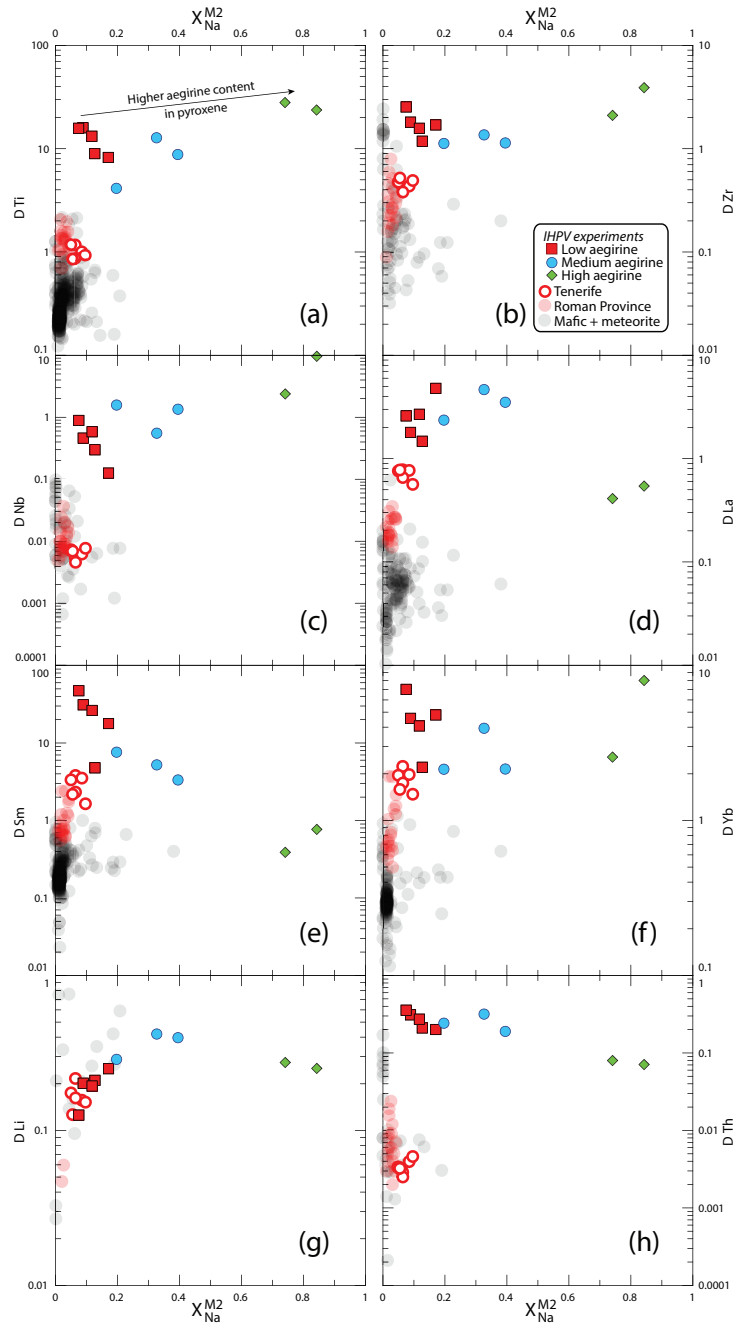


Figure S5: Element partitioning coefficients for HFSE (Ti, Zr, Nb), REE (La, Sm, Yb) and TE (Li, Th) vs.  $X_{Na}^{M2}$ . Literature values ( $n = 411$ ), including those from the Roman Province, Italy, are from the compilation of Bédard (2014).

<sup>1416</sup> **8. Electronic appendices**

xlsx

Table S1: Electronic appendix (.xlsx file) containing experiment starting glass compositions, experiment run conditions, mineral abundances in experimental charges, compositions of reference materials used for EPMA and LA-ICP analyses, major-element concentrations for experiment glasses and clinopyroxene, partition coefficients and fitted lattice-strain parameters.

kml

Table S2: Electronic appendix (.kml file) containing field locations for the Canary Islands samples.

kml

Table S3: Electronic appendix (.xlsx file) containing electron-microprobe transects across experiment clinopyroxene for Ce, Mg and Fe. The data indicate that  $D_{Ce}^{px/melt}$  values determined from our experiments are overestimates, but only by up to 25%. Sector zoning in the clinopyroxene appears to have a larger impact on apparent Ce partitioning behaviour than growth zoning.

pdf

Table S4: Electronic appendix (.pdf file) containing multiple linear regression reports from the stepwise fitting of 3+ cation lattice-strain parameters for the predictive model for element-partitioning (39 pages).

xlsx

Table S5: Electronic appendix (.xlsx file) containing a numerical model for prediction of clinopyroxene/melt element-partitioning coefficients for ions of 3+ valence. Required input data are major-element oxide compositions for clinopyroxene, pressure and temperature. The model for the M2 site is calibrated for application to systems of basaltic to peralkaline phonolite composition. The model for the M1 site is calibrated for use on alkaline to weakly peralkaline systems where the aegirine mol% in clinopyroxene does not exceed 50.